2021년 8월

석사학위 논문

Transition metal based free-standing membrane as a multi-functional electrode for Zinc-air batteries and water splitting

조 선 대 학 교 대 학 원

화 학 공 학 과

손 홍 진

Transition metal based free-standing membrane as a multi-functional electrode for Zinc-air batteries and water splitting

아연-공기 배터리 및 물 분해를 위한 다기능 전극으로 작동하는 전이 금속 기반 free-standing 멤브레인

2021년 8월 27일

조 선 대 학 교 대 학 원

화 학 공 학 과

손 홍 진

Transition metal based free-standing membrane as a multi-functional electrode for Zinc-air batteries and water splitting

지 도 교 수　　안 성 훈

이 논문을 공학 석사학위신청 논문으로 제출함

2021년 4월

조 선 대 학 교　대 학 원

화 학 공 학 과

손　　홍　　진

손홍진의 석사학위논문을 인준함

위 원 장 조선대학교 교 수 이 중 헌 (인)

위 원 조선대학교 교 수 이 정 수 (인)

위 원 조선대학교 교 수 안 성 훈 (인)

2021년 5월

조 선 대 학 교 대 학 원

C O N T E N T S

List of Tables

List of Figures

ABSTRACT

아연-공기 배터리 및 물 분해를 위한 다기능 전극으로 작동하는 전이 금속 기반 free-standing 멤브레인

Son, Hong jin
Advisor : Prof. Ahn, Sung-hoon, Ph.D.
Department of Chemical Engineering,
Graduate School of
Chosun University

전이금속 (Co, Ni, Fe, Mo)은 대표적으로 비-귀금속 촉매로 활용되는 물질이며 이는 직접적으로 활성점, 기판으로 이용된다. 이를 이용하여 직접적으로 사용이 가능한 코발트-질소-탄소 기반 계층적 구조를 가지는 촉매를 개발한다. 코발트는 간단한 공정과정을 통하여 표면의 개질(Co-N-C)이 이루어지며 이를 통해 산소 생산, 산소 환원, 수소 생산을 위한 낮은 과전압을 가진다. 간단한 공정을 통해 형성된 구조는 Scanning electron microscope (SEM), Transmission electron microscope (TEM)을 이용하여 구조분석을 진행한다.

탄소는 다양한 분야에서 이용되며 특히 높은 표면적은 촉매의 골격이 되기 위한 가장 적합한 물질로 활용된다. 질소와 탄소로 이루어진 멜라민과 함께 어닐링 과정을 거쳐 높은 효율성을 가지는 촉매적 성질을 가지게 되는 이 촉매는 수소생산반응 (10 mA cm^{-2}) 에서 36 mV, 산소생산반응 (10 mA cm^{-2}) 에서 229 mV의 매우 효율적인 과전압을 가지며, 알칼라인 전해질에서 1.51 V의 전압을 나타낸다.

또한, 산소환원반응에서 0.858 V의 하프-웨이브 포텐셜을 가진다. 각 반응에 대한 안정성 시험은 각각 40시간 이상 진행되었으며 적은 과전압의 차이를 가지며 훌륭한 내구성을 나타낸다.

수소 및 산소 생산에 적은 과전압을 요구하는 우수한 멤브레인 촉매는 직접적으로 아연-공기 배터리에 적용하여 사용이 가능하다. 액체 상태의 전해질에서 충·방전 전압의 차이는 0.92 V (2.10 V - 1.18 V)를 나타내며 고체 상태의 전해질에서 충·방전 전압의 차이가 0.5 V 이하로 매우 낮은 전압 차이를 보인다. 이는 코발트-질소-탄소 기반의 촉매가 활성점으로 직접 수소 및 산소 생산에 적극적으로 작용하며 충분한 에너지 장벽을 낮추는 다기능성 전기촉매 임을 알 수 있다.

Keywords: electrocatalyst, free-standing, multi-functional, Zn-air batteries, hierarchical structure

I. Introduction

A. Background of Study

The consumption of conventional energy source such as coals, oils, and fossil fuels is increasing explosively. These energy sources have a serious problem of environmental pollution in which CO_2 are emitted during the combustion process and are also the main culprit of global warming. For this reason, the conventional energy are converting from an renewable, eco-friendly, stable, and efficient energy source such as solar cells, fuel-cells, water-splitting system, metal-air battery. [1-3]

With the development of the fourth industry, the need for energy storage increases and demands more efficient and reliable performance. In addition, studies are conducted on various batteries with flexible properties for wearable devices and excellent performance. The electronic devices in real life utilize lithium-ion batteries the most because of high current density, light weight, long cycle performance, and high efficiency. However, lithium-ion batteries have critically several problems such as unstable, high price, poor durability. [4-5] A new generation (metal-air batteries) of batteries needs to be developed to compensate for the lithium-ion problems. Especially, zinc-air batteries (ZABs) are appropriate the substitute energy storage system due to low cost, high capacity, and superior durability.[6]

The hydrogen evolution reaction and oxygen evolution reaction of using a overall water-splitting contain the value as a ultra eco-friendly energy. In order to use green energy, HER, OER, and ORR are very important. [2] However, overalll water splitting is required a high overpotential, so the presence of a catalyst to solve this critical problem is essential. The noble metal (e.g., Pt/C, IrO_2, Ru/C)-based catalysts required the low-overpotential. For this reason, the noble-based catalysts are used the most in the industry. For example, Platinum has very high selectivity in HER, and iridium and ruthenium exhibit superior performance in OER, but high costs due to scarcity. [7-8] In addition, the conventional method for fabricate an electrocatalyst using the substrate and powder-type catalyst materials is required. The mono-functional catalyst and complex process of production is induce the increase cost. Therefore, the development of a self-assembly bi-, tri-functional electrode is essential for efficient production of catalyst.

For these reasons, the study of M-N-C (M = Co, Ni, Fe, Mo) based electrcatalsts using non-noble metals for the HER, OER, and ORR. [9-11] M-N-C based electrocatalysts have a hierarchical structure and perform as a catalytic active sties by high conductivity, N-doped transition metals, resulting in similiar or superior performance to noble metal-based catalyst. [9]

Accordingly, in this study, a tri-functional (HER, OER, ORR) substrate free monolithic membrane type electrocatalyst is fabricated through facile process to develop efficient non-noble metal-based Co-N-C electrocatalyst. The fabricated electrocatalysts are undergone by typical 3-electrode system for performance test of HER, OER, ORR and optimized of a variety of variable (e.g., temperature of annealing process, thickness of Co-N-C catalytic membrane, amount of melamine).

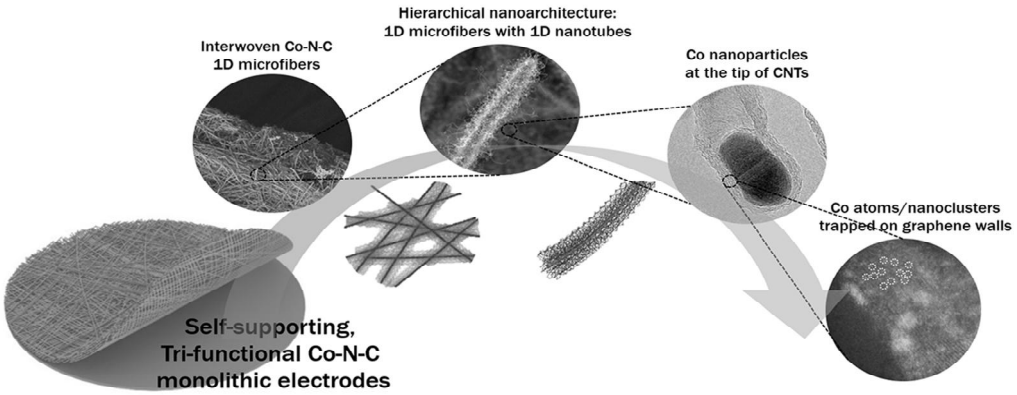

Figure. 1. Schematic illustration of procedures of Co-N-C catalytic membrane.

B. Background of Experimental

1. Cobalt of Transition Metal

Transition metals are positioned in 3 ~ 12 groups and 4 ~ 7 periods in the periodic table. The transition metals have 4 electrons for chemical bonding and can have an oxidation number of 4. The lone pair of electrons participating in the combining with elements such as oxygen, nitrogen, and sulfur, and is used as superior active points. For this reason, transition-metal based electrode exhibits a activity of electrochemical reaction.[1, 14] Furthermore, a transition metal-based non-noble metal electrocatalyst using carbon source such as Graphene, carbon nanotubes, carbon nanofibers and a metal-organic-framework as a substrate, which has an advantage of a large surface area, is being studied actively. [15, 16]

Cobalt, on of the non-noble metals, utilized to manufacture magnets and high-strength alloys on account of ferromagnetic and hard properties. Relatively inexpensive cobalt has been studied as an high-efficient electrocatalyst for overall water splitting and as and cathode for zinc-air batteries, and is used in a variety forms of bonding formation such as Co-N [2], Co-P [17], Co-O_x (or OH) [18, 19]. In particular, the existence of Co-N chemical bonds are form that can dramatically improve ORR.

The development of electrocatalysts with multifunctional characteristics is steadily progressing. Simulation using DFT played a major role in increasing the level of development of electrocatalyst and enabled experimental proof of single-atom catalysts through computational simulation. Therefore, It can be seen that an atomic level metallic cobalts are trapped at the edge of the graphene and showed as an active sites for effective overall water splitting. [20, 21] Among a varity of metals, cobalts has an advantage over the absorption-desorption energy for HER, OER, and ORR intermediates in studies based on DFT theory. [22]

2. Carbon Nanotubes

Carbon is a stable material and used in various dimensions of porous structures (e.g., graphene oxide, reduced graphene oxide, graphene, carbon nanotube), enabling effective utilize in OER. [12] The sacrificial substrate based on carbon has a superior charge transfer and mass transfer for water splitting, and air cathode of zinc-air battteries due to widely electrochemical surface area. Especially, carbon nanotubes grow through the diffusion of carbon surface at high temperatures and have a suitable structure for trap of metallic transition metals at carbon nanotube tips. [12, 13] Carbon nanotubes are growth on the metal precursor such as cobalt by mechanism of surface diffusion at high temperature (> 700 ^{o}C). [23]

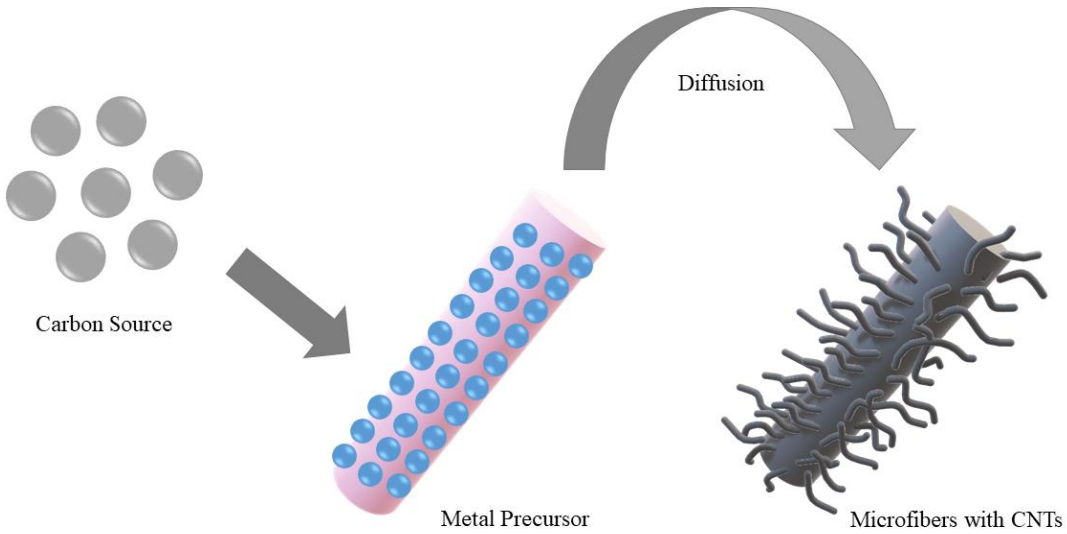

Figure. 2. Schematic illustration of diffusion mechanism by carbon source.

3. Melamine

Melamine is used for source of assist-materials for complex with transitional metals. It has insoluble property and aromatic ring structure consisting of amine and carbon. [24] The stable structure of melamine is decomposed at high temperature (> 450 °C), making a excellent source of nitrogen, and carbon. Decomposed nitrogen combines with a metallic metal precursor to form an M-N_x bond, and carbon grows into CNT according to the mechanism of diffusion, while simultaneously forming a variety of C-N such as pyridinic N, graphitic N, oxidized N and pyrrolic N. (Figure. 3) [24-26]

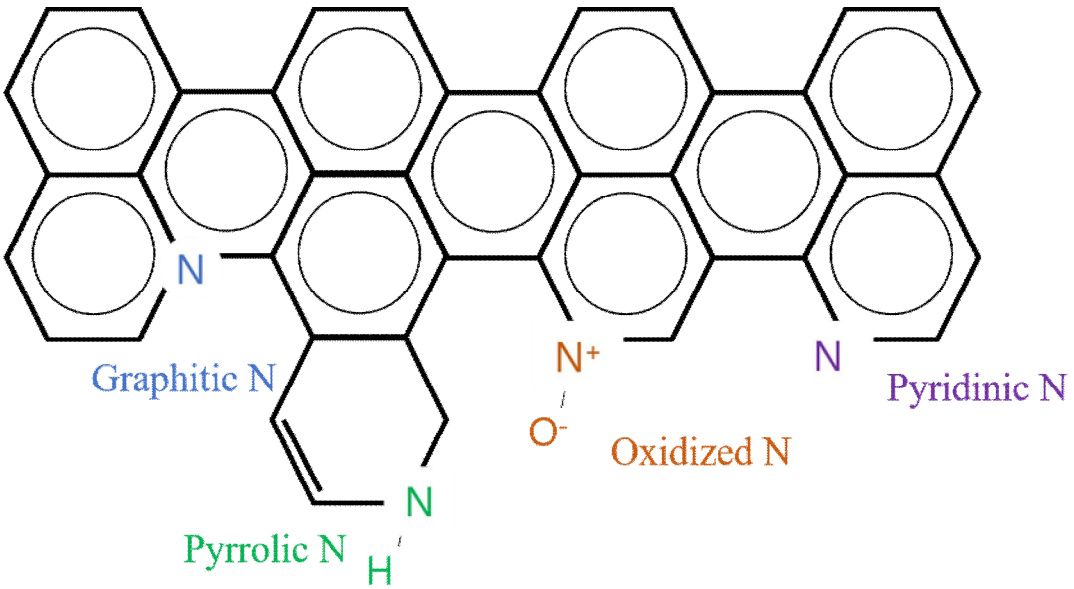

Figure. 3. Schematic illustration of C-Nx bonding.

4. Electrochemical Analysis

The electrochemical analysis is performed by bipotentiostat workstation. For measurement of electrochemical performance such as HER, OER, and OER is carry out with three-electrode system. The reference electrode is using a Hg/HgO with saturated 1 M NaOH, counter electrode is Pt wire, and catalytic membrane sample is utilized as working electrode. All of the measurement potentials are converted to V_{RHE} by the following equation.

$$V_{RHE} = V_{Hg/HgO} + (0.14 + 0.059 \times pH)\,V$$

All of the linear sweep voltammetry (LSV) measurement are proceeded after a stabilization phase of 50 cycles with potential range -0.4 ~ 0.05 V_{RHE} at HER, 0.6 ~ 1.0 V_{RHE} at OER, respectively. LSV curved are obtained with a scan rate 0.2 mV s-1 in 1 M KOH and iR 80 % compensated. Nyquist plot is obtained by EIS analysis with the frequency range 10^{6} ~ 10^{-1} Hz with an amplitude perturbation of 5 mV. The chronopotentiostat is analyzed at 30 mV cm^{-2}.

The ORR analysis is performed by RRDE in 0.1M KOH with O_2-saturated condition. The working electrode is fabricated by catalytic solution dispersing 10 mg of catalyst in 1.9 ml isopropyl alcohol containing 100 μL of 5 % nafion solution. The solution is mixed homogenously by sonication for 30 min. Afterwards, 20 μL of catalyst ink is dropped on the glassy carbon of ring-disk electrode and dried in the room temperature. The amount of loading is 100 μL cm^{-2}.

The electron transfer number is calculated following the Koutechy-Levich equation from LSV curve.

$$\frac{1}{J} = \frac{1}{J_L} + \frac{1}{J_K} = \frac{1}{B\omega^{1/2}} + \frac{1}{J_K}$$

$$B = 0.62nFC_o(D_o)^{2/3}v^{-1/6}$$

where J is the measurement of current density, J_k and J_L are the kinetic and

diffusion limit current density, respectively. ω is an angular rate, F is the Faraday constant (96485 C^{-1}), Co is initial bulk concentration, D_o is the diffusion coefficient of oxygen (1.9×10^{-5} cm^2 s^{-1}), and ν is the kinetic viscosity of the electrolyte (0.01 cm^2 s^{-1}).

The electron transfer number and yield of hydroperoxide are caculated from ring and disk current density (I_d and I_r) by the following equation.

$$n = \frac{4 I_d}{I_d + I_r / N}$$

$$\% H_2O_2 = \frac{2 I_r / N}{I_d + I_r / N} \times 100\%$$

where I_d is current density of disk, I_r is current density of ring, and N is the collection efficiency of RRDE (N = 0.37 with AFE7R9GCPT RRDE electrode, PINE research)

II. Experimental

A. Fabricated of Free-standing Catalytic Co-N-C membrane

1. Synthesis of Cobalt (oxy)hydroxide microfibers membrane

1.5 g of Cobalt (Ⅱ) chloride hexahydrate and 1.2 g nitrilotriacetic acid are dissolved in 80 ml aqueous solution containing 20 ml isopropyl alcohol with magnetic stirring homogenously at 25 ^{o}C. Afterward, the homogenous solution put into Teflon-lined autoclave and react in the oven at 200 ^{o}C for 24 h. After cooling at the room temperature, the fabricated product is washed with methaol and water several times. Finally, the product is fabricated of milky pink color membrane by vacuum filtration (Co-M)

2. Fabricated of Catalytic Cobalt-Nitrogen-Carbon monolith membrane

As Prepared Co-M is reconstruct by anneling process. The Co-M is placed on the alumina crucible and the melamine is placed on the another alumina crucible. All crucibles are arranged in lined in the quartz tube for annealing. The melamine is decomposed at 450 ^{o}C for 2 h with ramping rate of 2.5 ^{o}C, following the 600 – 1000 ^{o}C for 6 h with a ramping rate 5 ^{o}C under Ar-flow atmosphere. After reaction, the black color monolithic membrane is obtained, and directly used for electrochemical performance analysis as an electrode. For comparing, cobalt oxide is prepared at 350 ^{o}C for 3 h with a ramping rate 5 ^{o}C. The amount of melamine, intermediate temperature, and annealing temperature are considered for the most excellent electrode performance. The morphology of each catalytic membrane are observed and the electrocatalytic performance are measured.

3. Assembling the Zinc-Air Batteries

The electorde for liquid zinc-air battery is prepared by deposition of catalyst ink solution on the carbon paper with a loading amount of 1 mg cm^{-2}. For the all-solid-state zinc-air battery, the catalytic membrane air electrode is used directly and

zinc foil is utilized as anode for highly efficient rechargeable battery. The electrolyte of liquid-type is 6 M KOH solution containing 0.2 M zinc acetate. In solid-state battery, the electrolyte is prepared by poly(vinyl) alcohol gel with KOH. Battery cycling test is performed with discharging 300 s, following the charging 300 s, repeatly.

III. Results and Discussion

A. Charaterization of free-standing catalytic membrane

The catalytic membrane Co-N-C is fabricated by the hydrothermal process and annealing process with source of nitrogen and carbon. The hierarchical structure of catalyst is shown in Figure. 4. At first, the cobalt (oxy)hydroxide membrane is fabricated with cobalt (Ⅱ) chloride as a precursor and nitrilotriacetic acid as a agent of structure-form. The catalytic pink color membrane fabricated by vacuum filtration, following the annealing process with melamine of nitrogen and carbon source under Ar-flow atmosphere. The melamine is decomposed with carbon and ammonia gas above 350 ^{o}C and is induced the growing of CNTs at tips of metal precursor. [27] Therefore, the exist of melamine is critical factor for fabricating the highly efficient elecrode.

The membrane of Co-M is consist of smooth 1D structure with cobalt (oxy)hydroxide fibers by scanning-field emission microscope (SEM). The length of Co-M fibers is range of 200 ~ 300 nm and the diameter is 200 ~ 400 nm. The surface of Co-M membrane has a smooth texture in Figure. 5b and can see more detail nanostructures of Co-M in Figure. 5c. A variety of electrode are fabricated based-on the Co-M, which preserved this original structure.

At first, the Co-M membrane is annealed without melamine at 350 ^{o}C (Co-O_x). The membrane of annealed Co-O_x is reduced to the size because evaporate of the organic elements with annealing process under air flow. (Figure. 6) The nanostructure of Co-O_x nanowire is shown in Figure. 7a composed of nanoparticles average size of ~ 10 nm in Figure. 7b. We can obatain the acknowledge of producing a porous nanofiber during the annealing.

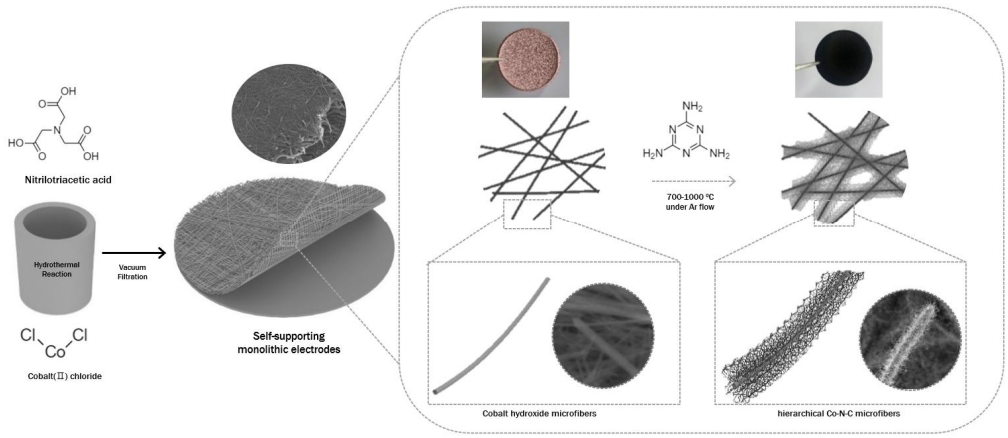

Figure. 4. Schematic illustration of the overall process of Co-N-C catalytic membrane.

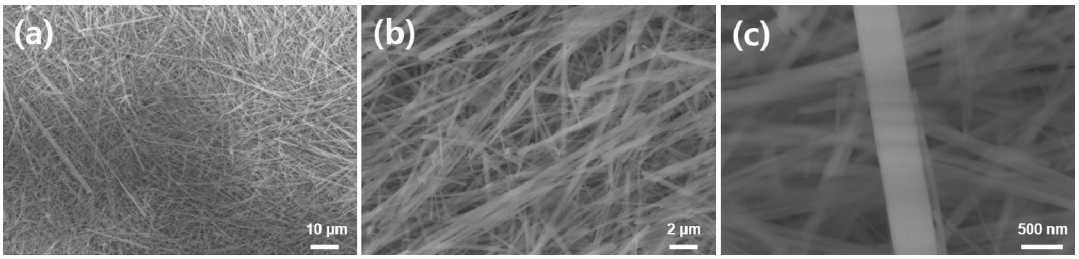

Figure. 5. SEM images of Co-M 1D nanofibers.

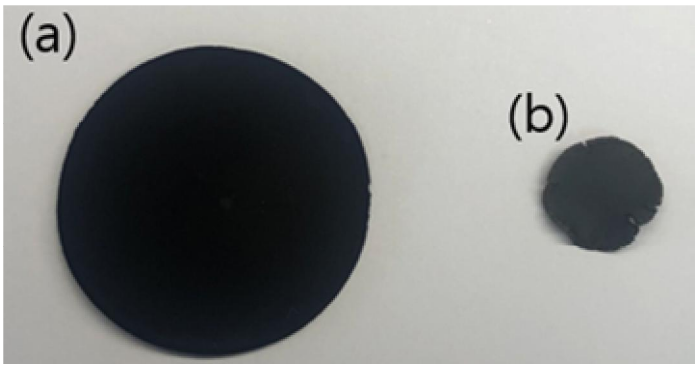

Figure. 6. Optical images of (a) annealed with melamine, and (b) annealed the absence of melamine.

Secondly, the Co-M membrane is annealed at 450 °C for 3 h and then at 600 – 1000 °C for 6 h with melamine. The annealed membrane (Co-N-C) is changing the pink to black color. (Figure. 8) This variation of color is that sufficient growth of CNTs is not proceeded in the presence of melamine. The surface of monolithic electrode, some damages are shown but without any cracks. (Figure. 7c) The mechanical properties to maintain the free-standing membrane derived-from interwovened 1D microfibers. (Figure. 7d) In contrast, the membrane of annealing without melamine is carried out the critical problem that not forming the CNTs and cobalt particles are agglomerated each others, and lost their structure. (Figure. 9) The effect of distance between melamine and membrane is fixed to prevent contact, which formed to micrometer scale wires. (Figure. 10)

To confirming the formation of a hierachical structure with various factor, controlled using a variety amount of melamine from 0.25 – 2.5 g, intermediate temperature (350 – 550 °C), and various temperature 600 – 1000 °C. During the annealing process, we confirmed that the temperature is a critical factor for formation of CNTs on the microfibers. At low temperature at 600 °C, The cobalt particles are embedded on the microfibers but the partial growth of CNTs is shown in Figure. 11a-c. During the annealing, when the higher temperature of annealing, the well-growth of CNTs is (Figure. 11d-i), but it aggregated gradually from 900 to 1000 °C. (Figure. 12) At 700 °C, the CNTs are growth evenly on the fibers and the length range of CNTs is 200 – 300 μm, well combined to each others. (Figure. 7e,f) All annealing process of intermediate temperature for stabilization is fixed at 450 °C. Because, when the low/high intermediate temperature at 350 °C / 550 °C (Figure. 13), the cobalt particles are aggregated evenly and a small amount of cobalt are trapped in the graphene of CNTs tips.

To confirm the effect of a mass of melamine, annealing are proceeded with various amount of melamine. With 0.2 g melamine, few CNTs are grow on the surface of Co-N-C microfiber (Figure. 14a,d) and cobalt matrix is observed in middle of CNTs (Figure. 15), indicating the cobalt particles are trapped in carbon. When a mass of melamine is increased from 0.4 g (Figure. 14b,e) to 0.6 g (Figure, 14c,f), the number of CNTs are increased gradually. More increasing the melamine with 0.75 g (Figure.

16a,d) and 1.0 g (Figure, 7e,f and Figure. 16b,e) at 700 °C denoted as Co-N-C-LM, respectively, the density of CNTs is very high compared to low-amount of melamine. Further increasing the melamine 1.5 g, the microfibers are coverd with CNTs in Figure. 7g,h and Figure. 16c,f. When the melamine 2.5 g, the CNTs are anchored to the surface of microfibers, denoted as Co-N-C. (Figure. 17) More increased the amount of melamine, no siginicant change of morphology of Co-N-C microfibers.

The Co-N-C membranes can fabricated a various thickness, range of ~ 500 μm. (Figure. 7i) The thickness of Co-N-C membrane is controlled by the Co-N-C solution in the vacuum filtration process. (Figure. 18) The cross-secional SEM images of Co-N-C at high magnefication is obseved in Figure. 7i and the diameter of single nanowire and hireachical structure are shown ~ 750 nm in Figure k,i.

The 1D hierachical structure is observed in more detail by the transsmission electron microscope (TEM) in Figure. 19a. The trapped cobalt nanoparticles (Co-NPs) with tips of CNTs (Figure. 19b). In Figure. 19c, a distance of metallic cobalt is observed a 0.207 nm, which coressponding of (111) facet. In addition, the microfiber is observed in abbreviation-corrected scanning trasmission electron microscopy (AC-STEM) to identify the cobalt atoms in Figure. 19d. In Figure. 19e, trapped cobalt atoms evenly are comfirmed by the high-angle annual dark-field STEM (HAADF-STEM) image. It is confirmed that not only Co-NPs with crystalline (Figure. 20b) but also clusters (Figure. 20c). At the same time, the bamboo-liked 1D structures of cobalt embeded on the fibers are observed by the growth reaction of CNTs in Figure. 21. The HAADF-STEM image, in Figure. 19f, the elements of C, Co, N are confirmed, indicating the uniform distribution of each element on the Co-N-C microfibers.

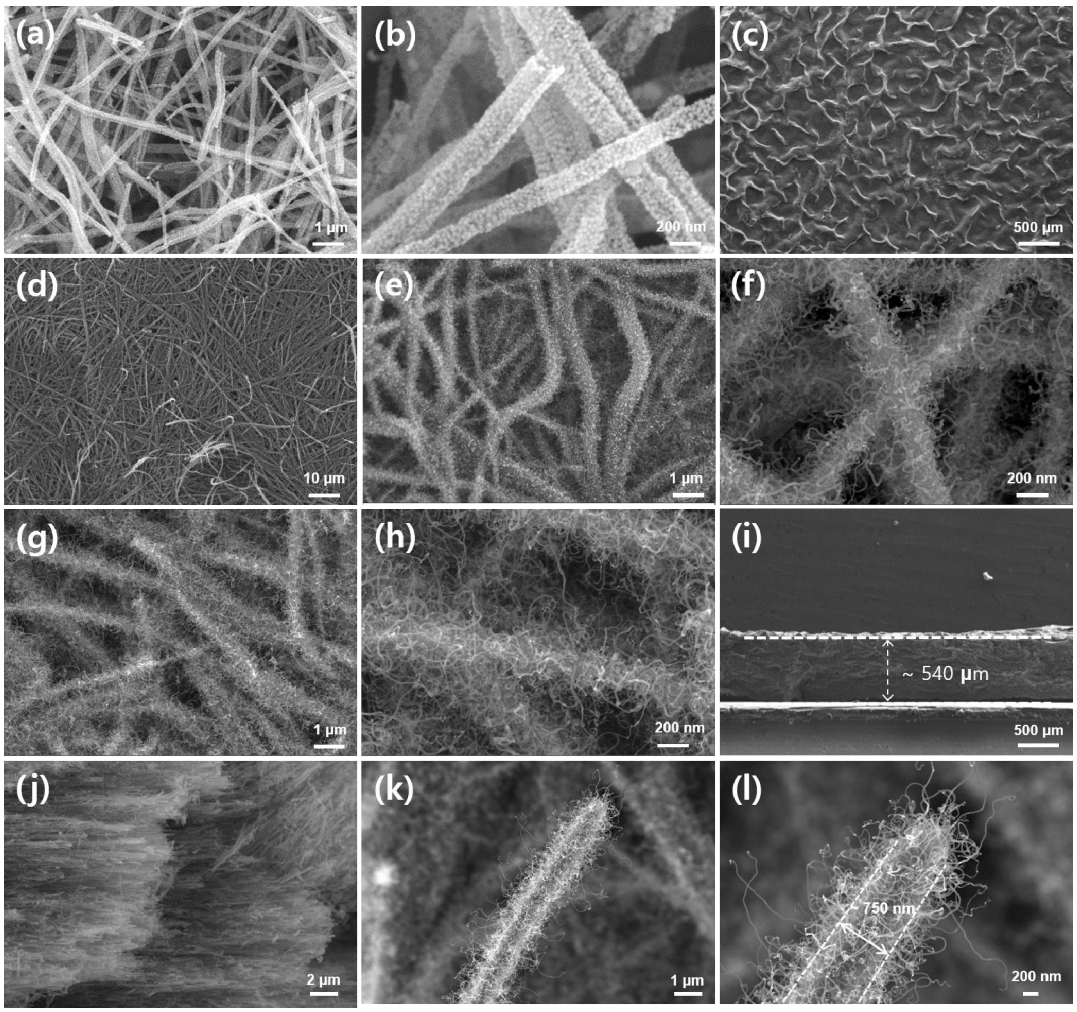

Figure. 7. (a,b) SEM images of Co-O_x, (c-f) Co-N-C-LM, and (g,h) Co-N-C sample. (i,j) Cross-sectional SEM images of Co-N-C, (k,i) Single nanowires of hiearchical 1D structure Co-N-C.

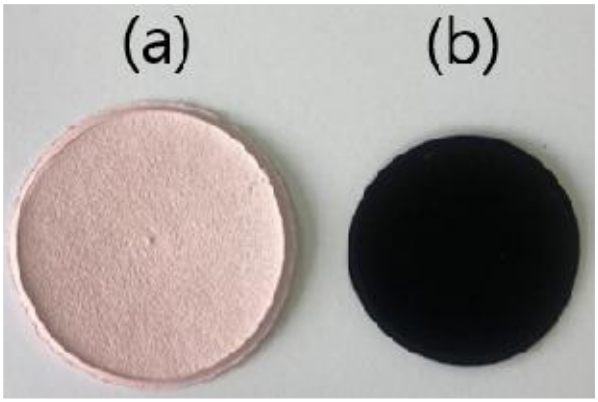

Figure. 8. Optical images of (a) Co-M membrane, and (b) annealed Co-N-C membrane with melamine.

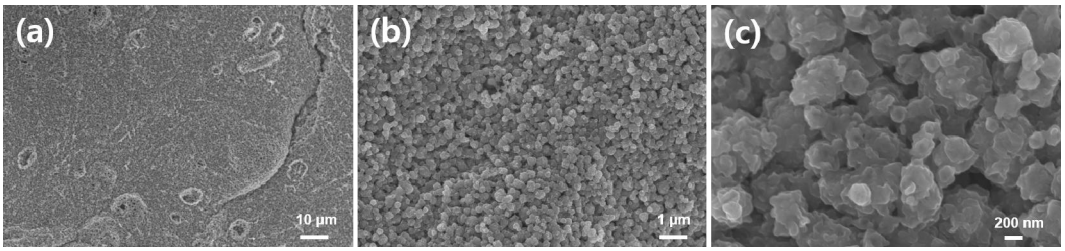

Figure. 9. SEM images of Co-O_x.

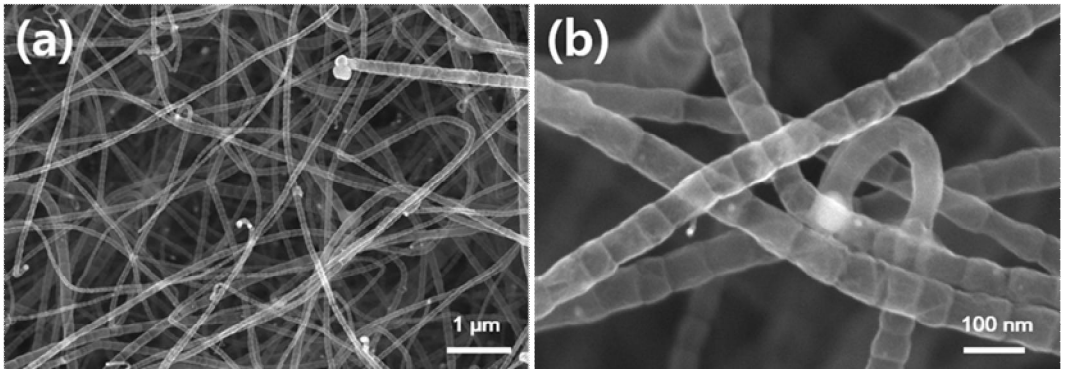

Figure. 10. SEM images of annealed Co-N-C with direct contact between melamine and membrane.

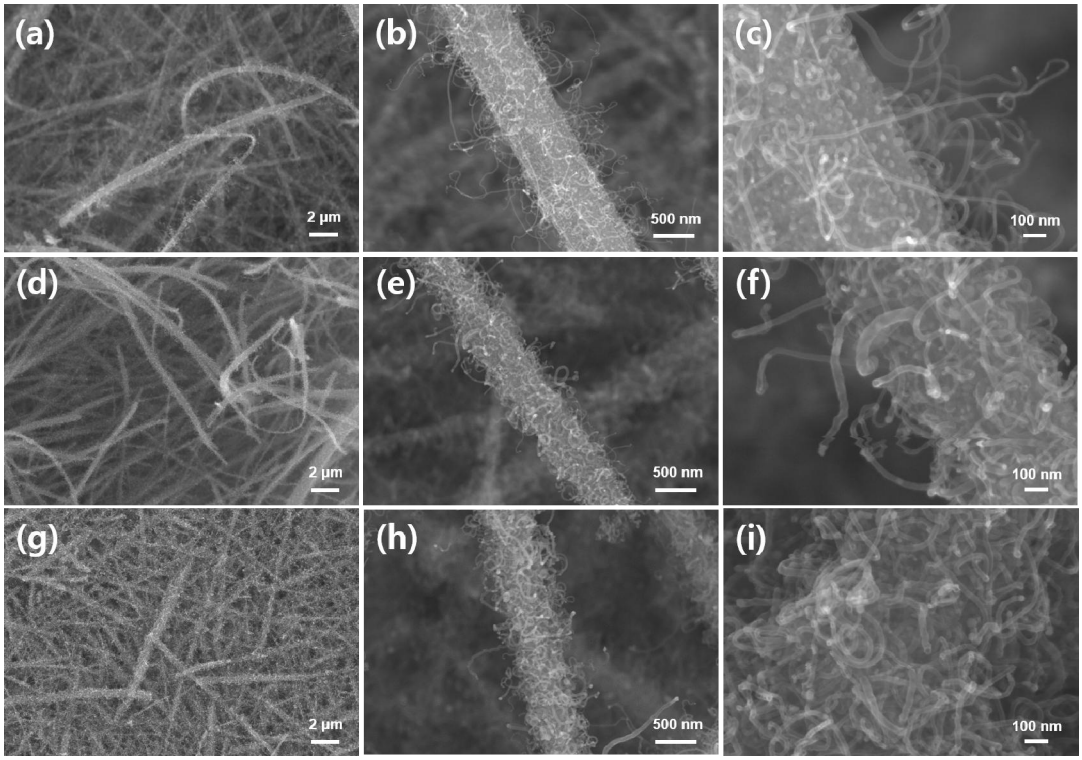

Figure. 11. (a-c) SEM images of Co-N-C membrane after annealing process with 600 °C, (d-f) 700 °C, (g-i) 800 °C.

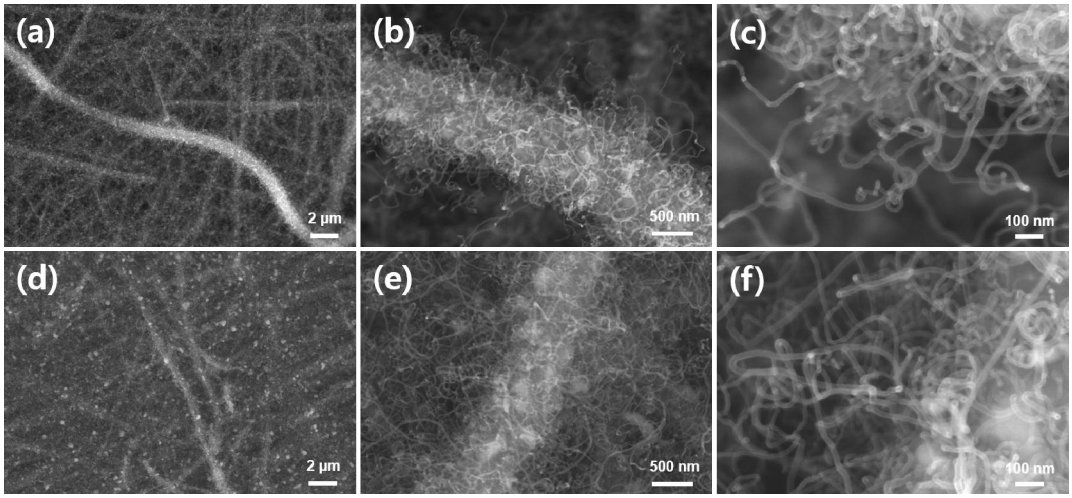

Figure. 12. (a-c) SEM images of Co-N-C membrane after annealing process with 900 ^{o}C, (d-f) 1000 ^{o}C.

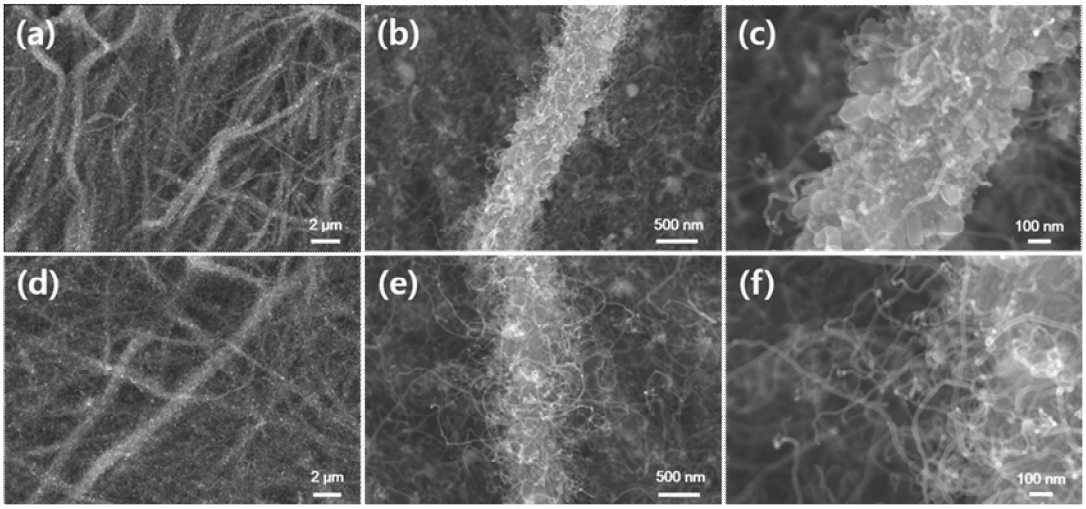

Figure. 13. (a-c) SEM images of Co-N-C membrane after annealing at 700 ^{o}C with the intermediate temperature at 350 ^{o}C, (d-f) 550 ^{o}C for 3 h.

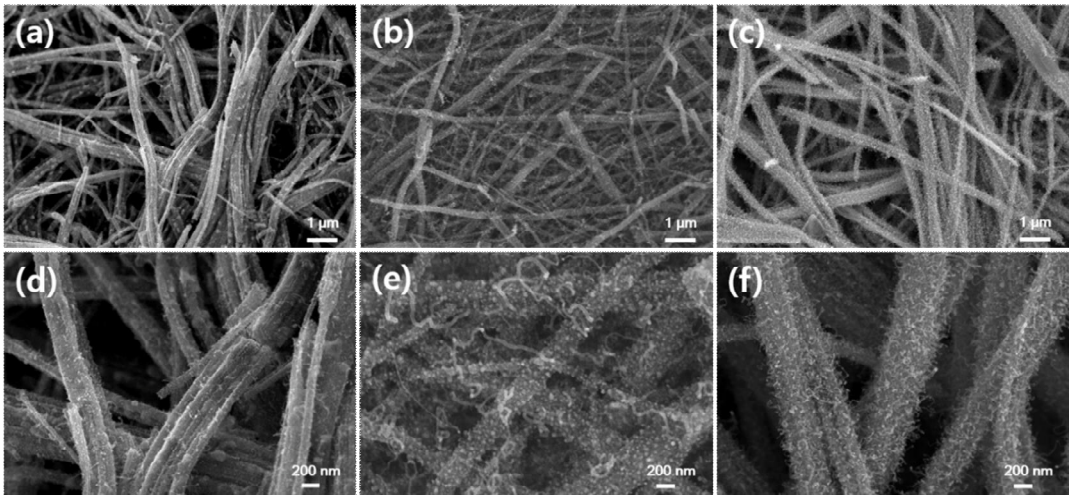

Figure. 14. SEM images of Co-N-C membrane after annealing with the amount of melamine (a,d) 0.2 g, (b,e) 0.4 g, and (c,f) 0.6 g.

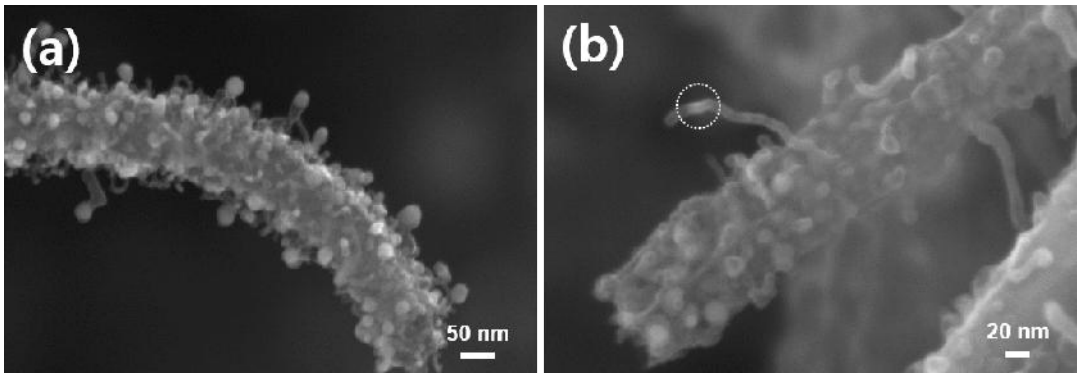

Figure. 15. (a,b) SEM images of Co-N-C membrane after annealing with many of melamine at high-magnification.

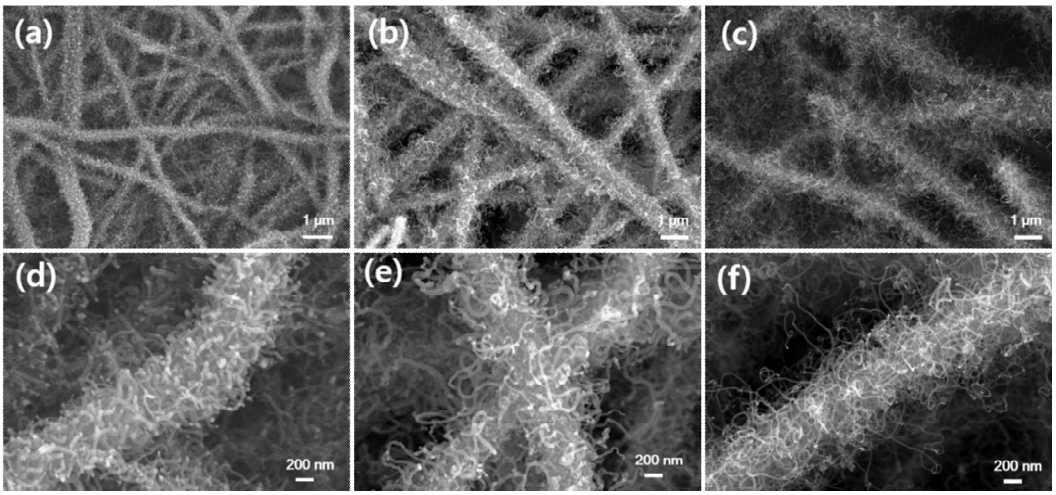

Figure. 16. (a,d) SEM images of hierachical Co-N-C membrane after annealing with melamine 0.75 g, (b,e) 1.0 g, (c,f) 1.5 g.

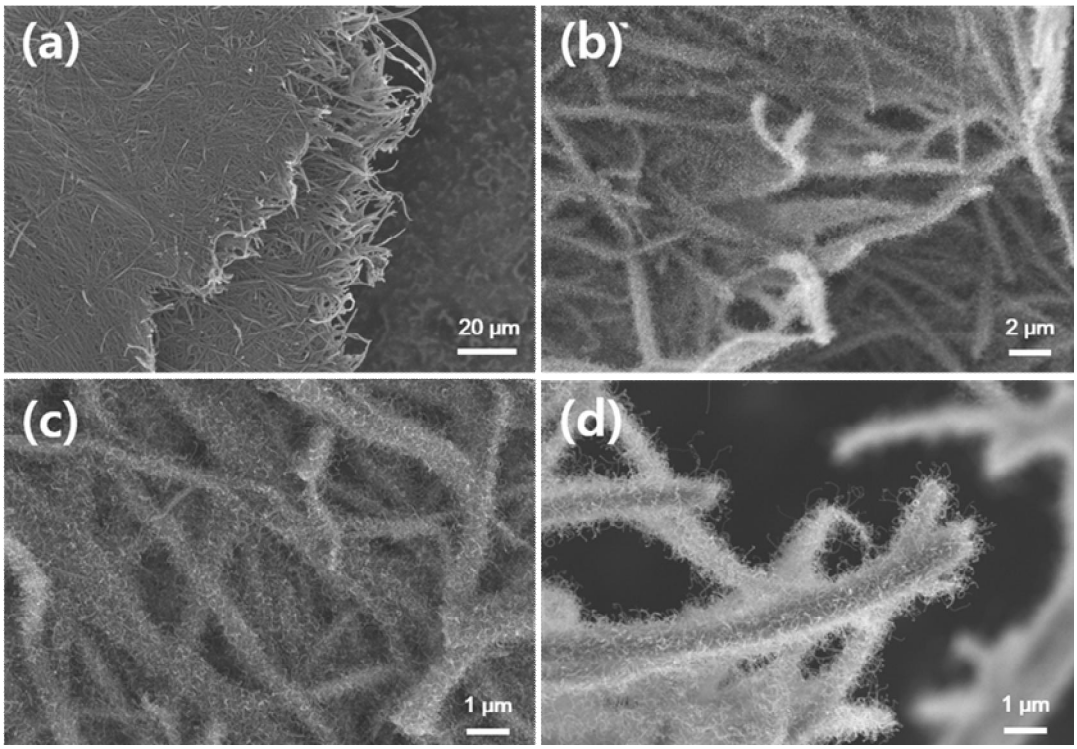

Figure. 17. (a-d) SEM images of Co-N-C membrane after annealing at 700 °C with the melamine 2.5 g.

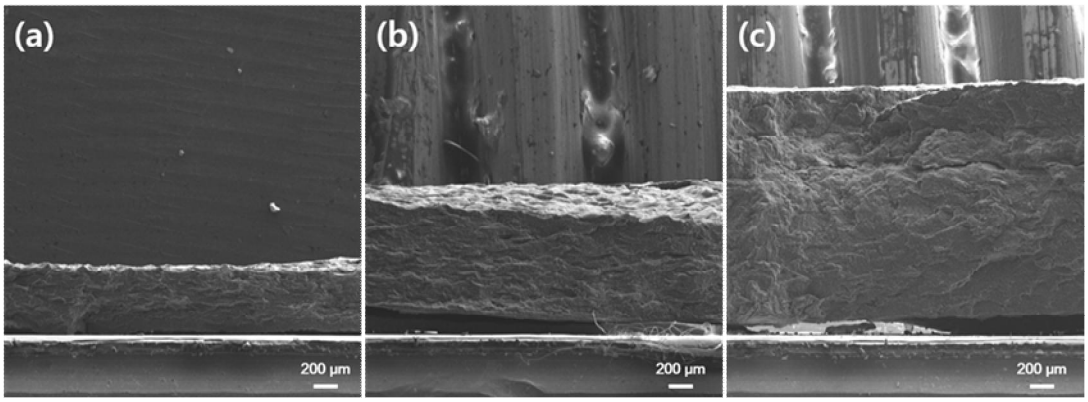

Figure. 18. (a-c) Cross-sectional SEM images of Co-N-C membrane with various thickness.

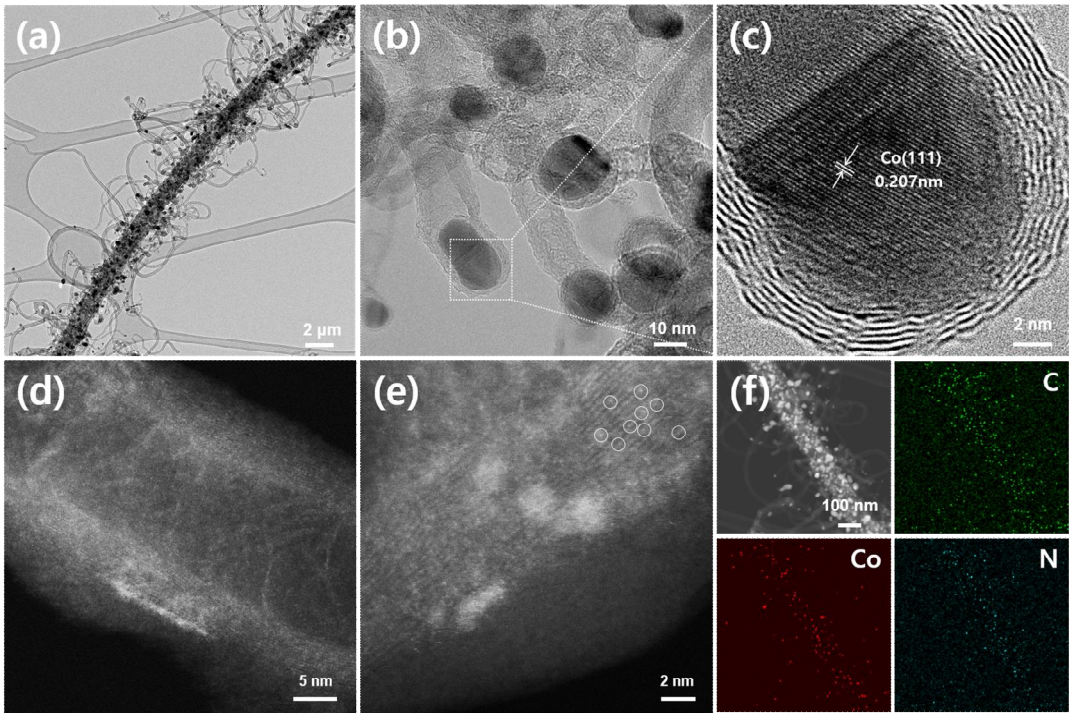

Figure. 19. (a,b) EF-TEM images of Co-N-C, (c) High-resolution TEM image of metallic cobalt at tips of CNTs. (d) AC-STEM image of CNT, and (e) STEM image of atomic-scale cobalt in graphene layer. (f) HADDF-STEM image of Co-N-C microfibers and EDS-mapping images of C, Co, N, respectively.

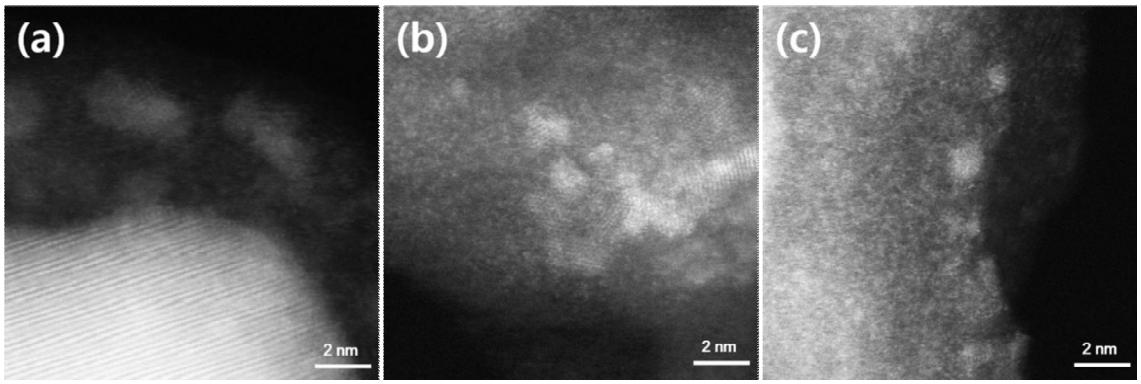

Figure. 20. (a-c) AC-STEM images of Co-N-C microfibers.

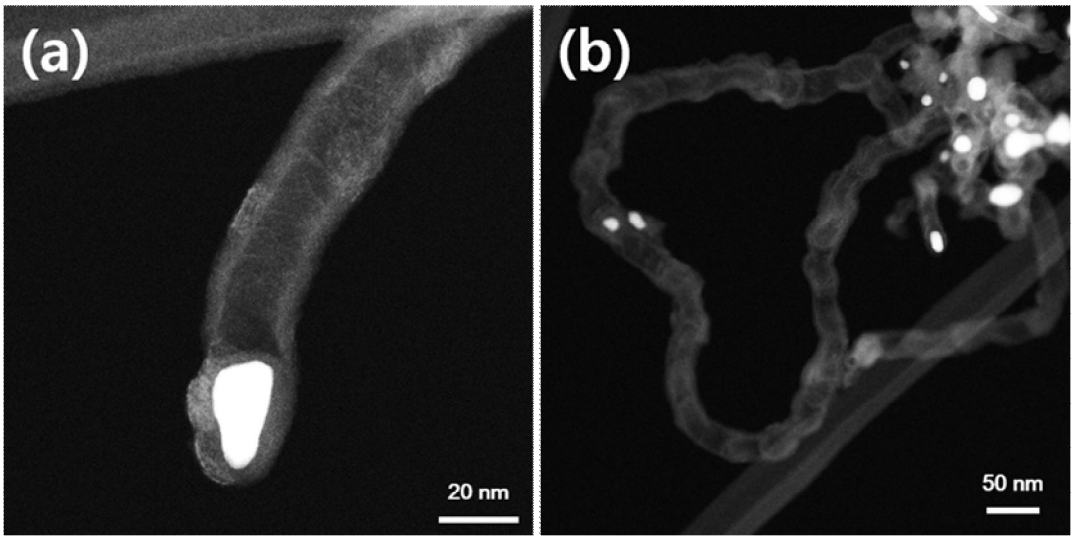

Figure. 21. (a,b) AC-STEM images of Co-N-C nanotubes.

The Fourier-transform infrared spectroscopy (FT-IR) spectra is superior method to comfirm an organic-inorganic materials. The FT-IR spectra of Co-N-C in Figure. 22, corresponding to smilar peaks in previously reported studies. [28, 29] The crystalline structure of Co-M is analyzed by X-ray diffraction (XRD). The as-fabricated Co-M membrane exhibits the strength of peak indexed to (0 0 3) plane of α-$Co(OH)_2$. (Figure. 23a, ICDD No. 46-0605) [30, 31] and it is disappeared by the growth of CNTs in the presence of the carbon source. The XRD pattern of Co-N-C is exhibits the peak of 44°, corresponding to metallic cobalt specie in Figure. 24a. (ICDD No. 15-0806) The increase of the main carbon peak intensity indexed to (0 0 2) plane at 26°, corresponding to the increased annealing temperature above 700 °C. Additionally, the peaks of Co_3O_4 are observed (ICDD No. 01-071-0816) in Figure. 24b, corresponding to Co-O_x. The successful formation of binding between elements during the annealing process with melamine is confirmed by X-ray photoelectron spectroscopy (XPS) survery. The intensity of carbon at Co-N-C membrane (Figure. 25b) is significantly strong compared to the Co-M membrane (Figure. 25a). Furthermore, the oxdiated carbon (Figure. 26a) and cobalt species indexed to $Co(OH)_2$ (Figure. 26b) are investigated. To compared to Co-M spectra of carbon, the high resolution peaks of two binding, corresponding to -C-O-C at 286.7 eV and -O-C=O at 288.9 eV due to formation of carbon matrix during the annealing process with carbon source from melamine and the -C-C peak is transformed at ~ 284.4 eV in Fiugre. 26c. [32, 33] As shown in Figure. 24b, The Co 2p spectra of Co-N-C three-peaks is observed, corresponding to metallic Co, Co^{2+}, and Co^{3+} at 778.2, 780.0, and 781.7 eV, respectively, with stallites peak at 785.2 eV. [34-37] Furthermore, the binding energies of N_2-species are comfirmed in Figure. 24c, the three peaks of N_2, corresponding to pyridinic N, metal(Co)-N_x, and graphitic N at 398.3, 399.6, and 402.3 eV, respectively. [33, 38] For analyzed the graphitized CNTs, the Raman spectroscopy is proceeded, following the I_g/I_d values obtained of the as-prepared Co-N-C membrane. The values of Co-N-C-600, 700, and 900 °C are 0.98, 1.00, and 1.08, respectively, corresponding to the higher the annealing temperature is, the higher the graphization is. These results are consistent with the SEM images of 600 to 900 °C.

The N_2 adsorption-desorption isotherm curves of Co-N-C samples are shown in Figure. 24e. The specific surface area of the Co-N-C electrdoes by different annealing temperature 600, 700, 800, and 900 ^oC are calculated to 151.5, 151.9, 99.3 and 94.1 $m^2\ g^{-1}$, respectively. The pore size distribution curve is analzed based on the non-local density functional theory (NLDFT) for 600 ^oC membrane and other 700, 800, and 900 ^oC samples. Remarkably, Co-N-C sample at 600 ^oC is smaller size distribution, corresponding to the non-efficient growth of CNTs. (Figure. 24f)

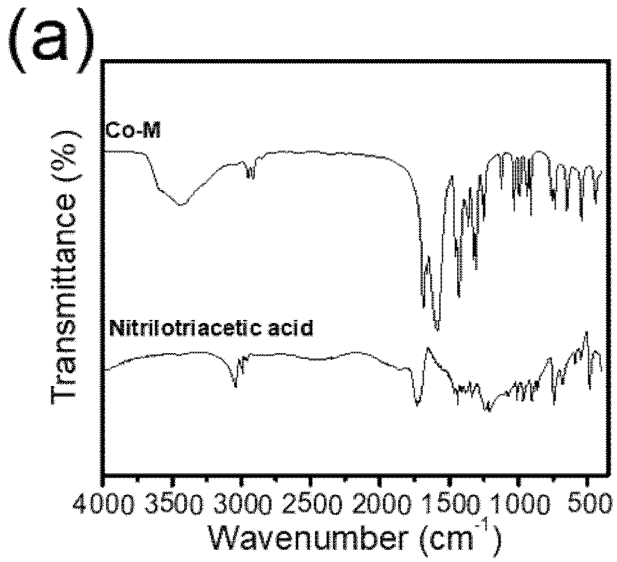

Figure. 22. (a) FT-IR spectra of Co-M.

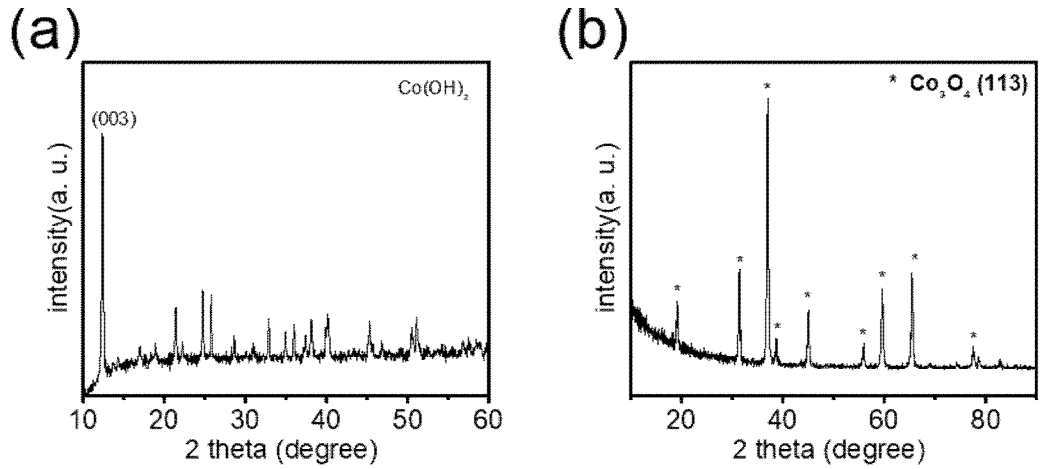

Figure. 23. (a) XRD pattern of Co-M, (b) annealed Co-M under air flow.

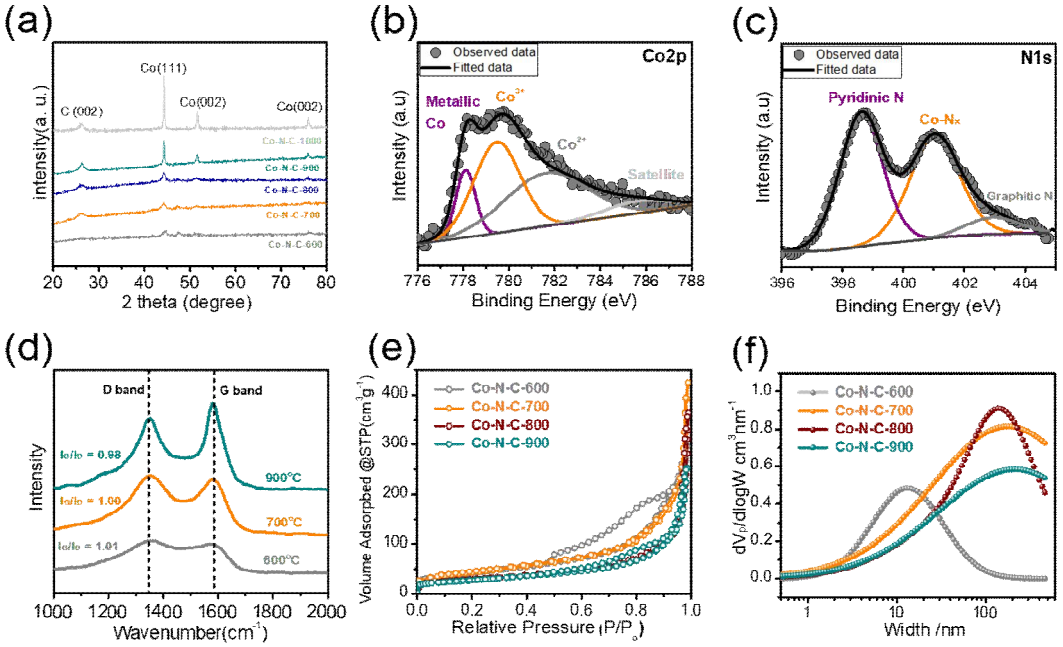

Figure. 24. (a) XRD pattern of different annealing temperature, respectively, (b) XPS spectra of Co, (c) N of Co-N-C. (c) Raman spectra of Co-N-C-600, 700, 900. (e) N_2-adsorption-desorption curves of Co-N-C, and (f) the corresponding pore size distribution.

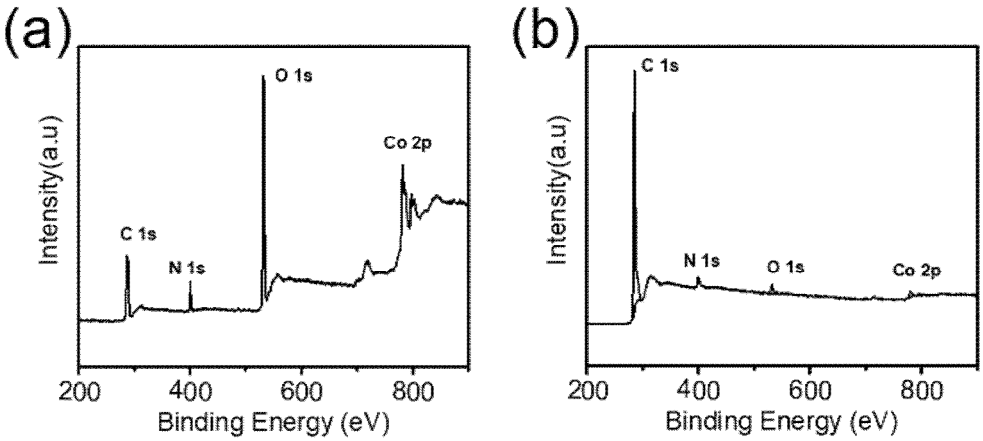

Figure. 25. (a) XPS survey spectra of Co-M, (b) Co-N-C.

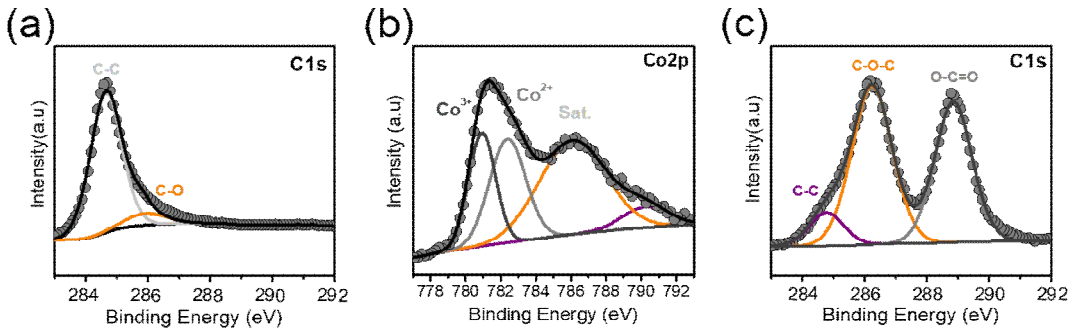

Figure. 26. (a) XPS spectra C1s, (b) Co2p 3/2 of Co-M, and (c) C1s of Co-N-C.

B. Electrochemical performance of Co-N-C electrode

In this part, a variety of parameters are considered to analyze the optimizing an electrocatalytic electrode for tri-functional performance. Firstly, variation of annealing temperature is considered to confirm the tri-functional performance according to the growth ratio of CNTs. (denoted Co-N-C-T, T = 600, 700, 800, 900, and 1000 ^{o}C) In Figure. 27a, the HER LSV curve of Co-N-C-600 is showing the inferior performance comparing the other annealing temperature samples. The required overpotential of Co-N-C-600 is 137 mV at the current density 10 mA cm^{-2}, which is even higher than others. The similar trend is investgated at the OER LSV curves in Figure. 27b. The inferior performance of Co-N-C-600 is due to insufficient growth of CNTs, confirmed by XRD peaks intensity of carbon, and Raman analysis. The required overpotential of various annealing temperature is imply that Co-atoms are utilized with the electrochmical performance and fully covered by the graphization of CNTs during the annealing process. Therefore, the electrochemical impedence spectroscopy (EIS) is conducted to confirm the role of graphited CNTs at the HER, and OER performance. In Figure. 27c, the Co-N-C-600 sample show the largest charge transfer resistance (R_{ct}), corresponding to the required overpotentials at the HER, and OER. On the other side, the Co-N-C-700 electrode show the most efficient performance of 64 mV for HER, 244 mV for OER at the current density 10 mA cm^{-2}. For this reason, the annealing temperature of Co-N-C is fixed the 700 ^{o}C for the folllowing electrochemical test.

Secondly, the mass of melamine is considered for optimizing the bi-functional performance. In Figure. 27e, melamine 2.5 g is the best condition for the bi-functional electrode in HER LSV. On the contrary, no significant activities are shown in OER activity. (Figure. 27f) More increased the amount of melamine, no siginicant performance of activity of Co-N-C electrode. In conclusion, we fixed the mass of melamine with 2.5 g. Finally, the increasing a well-growth of CNTs led to some increase in HER activity. (Figure. 28a) For this reason, the thickness of the Co-N-C is adjusted to ~ 1 mm.

In conclusion, the optimized electrode of the Co-N-C is choosen for comparison with benchmarking eletrocatalysts. Also, the scan rate with 0.2 mV s^{-1} is adjusted for faradic current, and to prevent overprizing the catalytic activities of Co-N-C electorde. (Figure. 29)

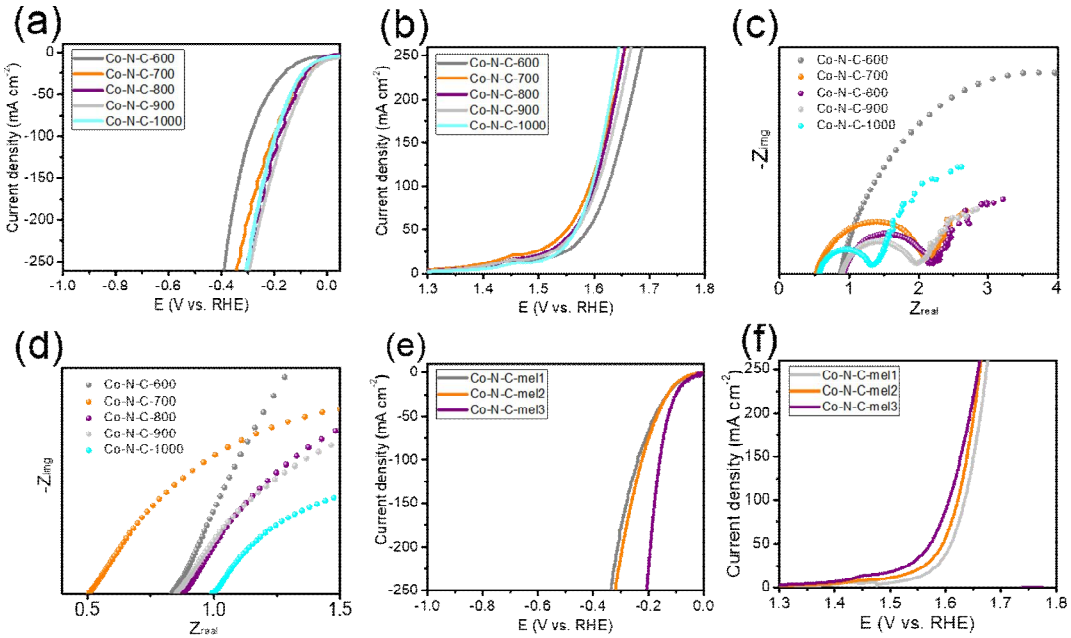

Figure. 27. (a) HER LSV of Co-N-C-T (T = 600 ~ 1000 °C) in 1 M KOH with the scan rate of 0.2 mV s^{-1}, (b) OER LSV of Co-N-C-T. Nyquist plots of Co-N-C (c) toward HER, (d) toward OER. The LSV curves of the amount of melamine at the annealing process (e) toward HER, (f) toward OER.

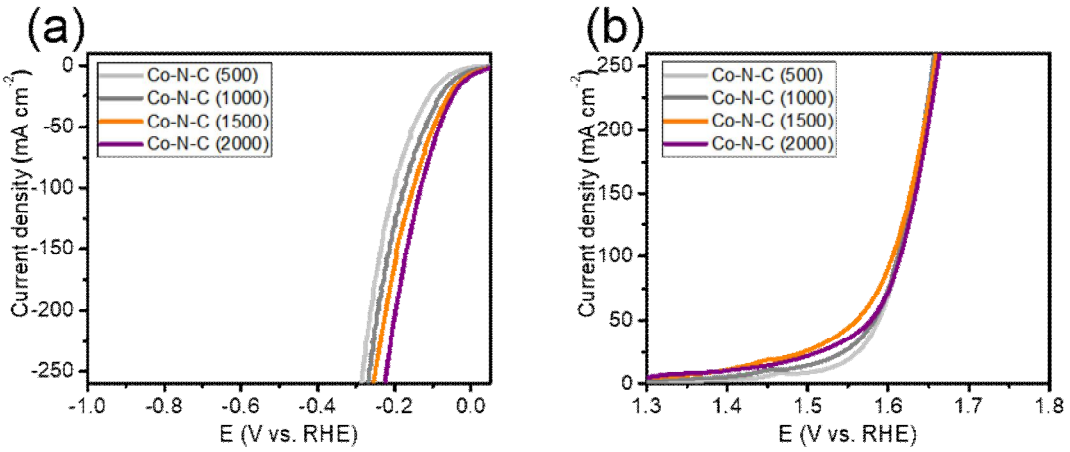

Figure. 28. LSV curves of Co-N-C (T), thickness (T) = 500, 1000, 1500, and 2000 μm, respectively. (a) toward HER, and (b) toward OER.

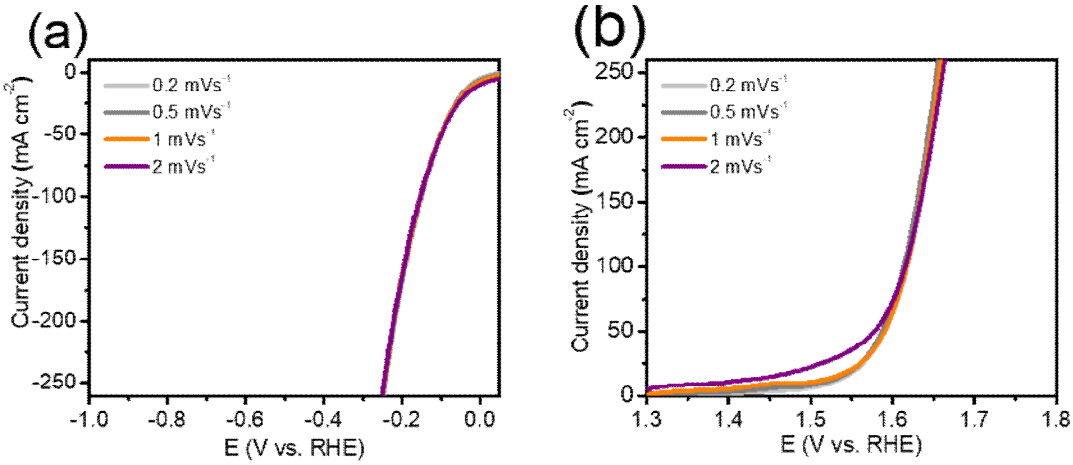

Figure. 29. LSV curves of Co-N-C (T), T = 500, 1000, 1500, and 2000 μm, respectively. (a) toward HER, and (b) toward OER.

The LSV curves of Co-N-C and Pt/C is conducted for comparison with HER in 1 M KOH electrolyte, as shown in Figure. 30a. As we know, the melamine mass is used to 1.0 g (Co-N-C-LM) and 2.5 g (Co-N-C). The Co-O_x exhibits the low activity with HER overpotential of 384 mV at the current density 10mA cm^{-2}, according to the addition of melamine leading to the growth of CNTs. To comparison of Co-O_x, the Co-N-C-LM requires the overpotential for HER at 10 mA cm^{-2} is 64 mV, and Co-N-C is 26 mV, which is close to the Pt/C of the bechmarking electrode for HER. (24 mV)

At a high current density at 100 mA cm^{-2}, required overpotenntials of Co-N-C-LM is 175 mV or Co-N-C is 127 mV are smaller than that of Pt/C (189 mV). The low overpotential exhibits the electrocatalytic surface-friendly properties, and leading to the minimization of interfacial resistance between substrate and nano-particles for active sites. However, the interfacial resistance of Pt/C produced by substrate (e.g., carbon paper) and binder material (e.g, Nafion), which hinder the facile mass/charge transfer between the consist of electrode.

In the tafel plot, the value of Co-O_x slope about 93.2 mV dec^{-1}, following slope value of Co-N-C and Co-N-C-LM reduced by the formation of CNTs. The tafel slope of Co-N-C-LM (87.5 mV dec^{-1}) and Co-N-C (53.7 mV dec^{-1}), which is comparable value of Pt/C slope, corresponidng to 44.6 mV dec^{-1} in Figure 30a,b. It indicate that mechanism of HER following a Volmer-Heyrovsky mechanism. [39, 40] Also, the OER activity is investigated in 1 M KOH electrolyte at 10 mA cm^{-2} with 0.2 mV s^{-1}. The trend of OER activity is similar to that of HER activity. In Figure. 30c, the activity of Co-O_x exhibits the poor efficiency, following improve that reconstructed by the annealing process in the prsence of melamine. The activity of Co-N-C-LM is required at 229 mV at 10 mA cm^{-2}, and 416 mV at 100 mA cm^{-2}, which is more efficient than control sample of IrO_2 electrode. The optimized Co-N-C electrode exhibits an overpotential of 260 mV at 10 mA cm^{-2}, 416 mV at 100 mA cm^{-2}, which this value of overpotentials surpaass the IrO_2 electrode activity. These conclusion corresponding to Tafel plot in Figure 30d, superior activity of Co-N-C (139.9 mV dec^{-1}) compared to that of IrO_2 tafel slope (180.1 mV dec^{-1}). The conclusion of tafel slope exhibits the favorable electrode kinetics, which can be attributed to the facile mass and charge transfer for OER.

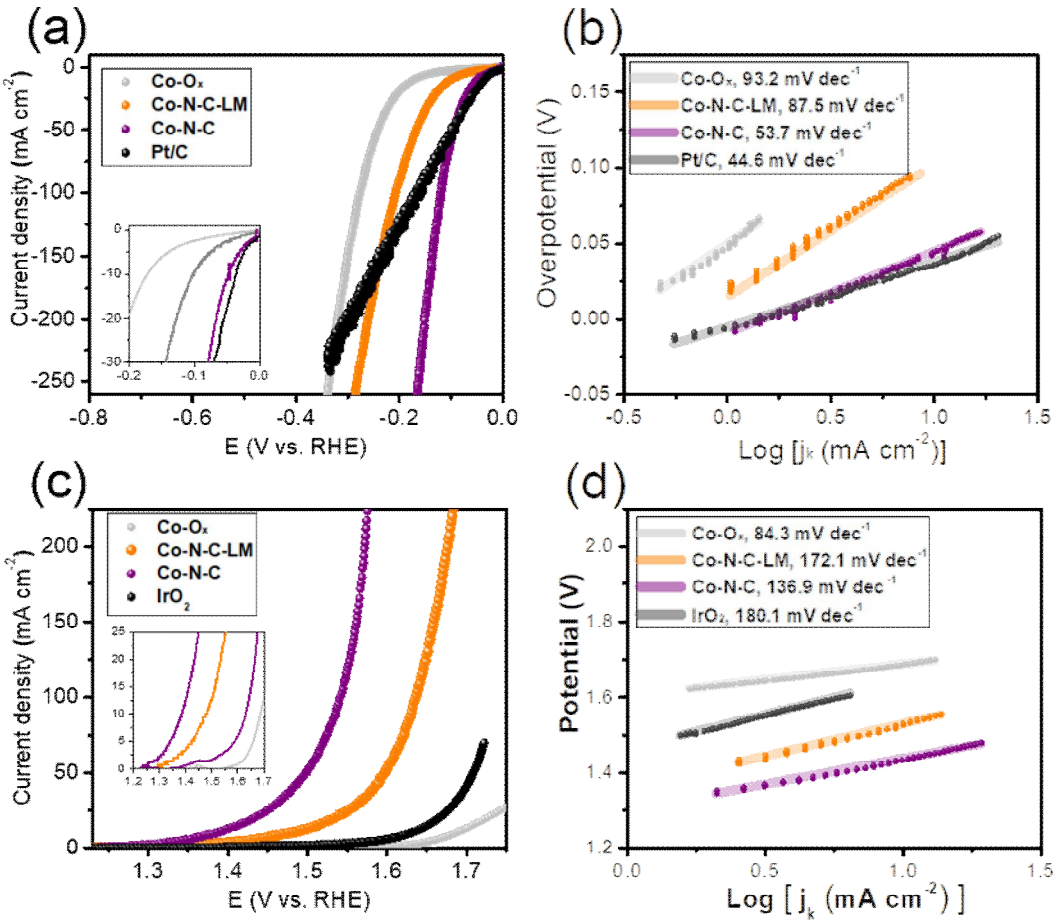

Figure. 30. LSV curves toward (a) HER, (c) OER. and Tafel plot toward (b) HER, (d) OER.

The density of hierachical structure by the CNTs further improved for HER and OER activities. The electrocatalytic activity can be traced by the formation of embedding Co atoms in the graphene with CNTs. In Figure. 31a, the Co-O_x monolithic electrode show the highest resistance not only contact but charge transfer (R_{ct}) compared to others. In contrast, Co-N-C electrode has lowest R_{ct} among the various samples, corresponding to the superior charge transfer between the Co-N-C fibers. A simliar Nyquist shape observed toward OER in Figure 31b, which indicates the good electron transfer by monolithic Co-N-C fibers, and contribute to the hierachical 1D nanostructure consist of carbon matrix. Furthermore, we perform the CV at the different rate of cycle scan for the estimation of electrochemical surface area (ECSA) of Co-N-C. (Figure. 32a) The C_{dl} of Co-N-C is a 207.8 mF cm^{-2}, showing a wide number of active sites on the surface of electrode. (Figure. 32b) The stability of each HER and OER conducts by chronopotentiostat test (*c-t* test) at current density 30 mA cm^{-2} for 45 h. In conclusion, the overpotential is no significant drop during the test, contain the required overpotential of ~ 78 mV toward HER and ~ 246 mV toward OER, respectively. (Figure. 33)

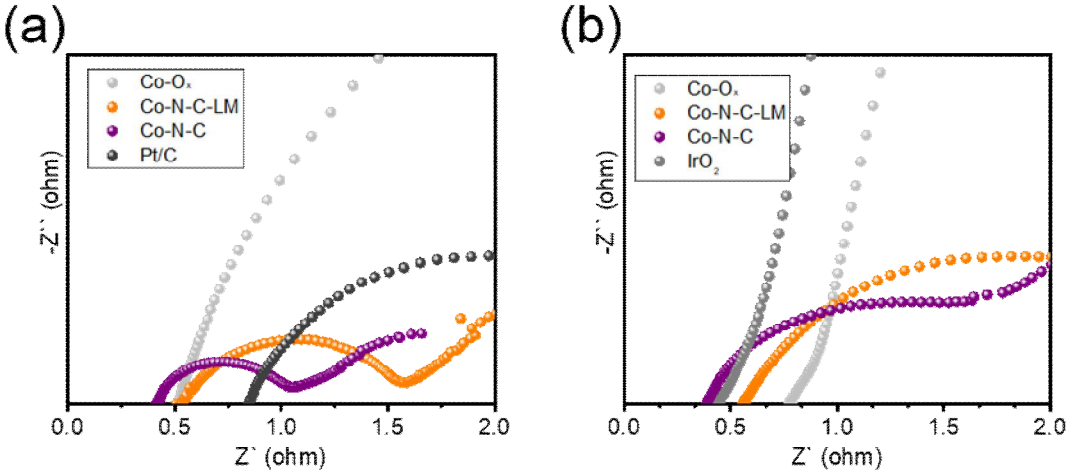

Figure. 31. Nyquist plot toward (a) HER, and (b) OER.

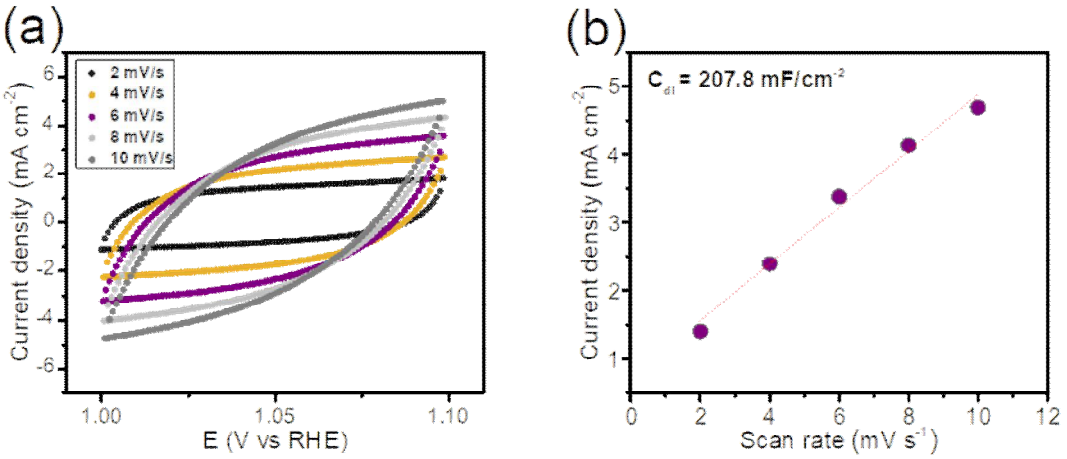

Figure. 32. (a) CV curves of Co-N-C with a non-fafadaic reaction region of 1.0 – 1.1 V, (b) C_{dl} value of Co-N-C.

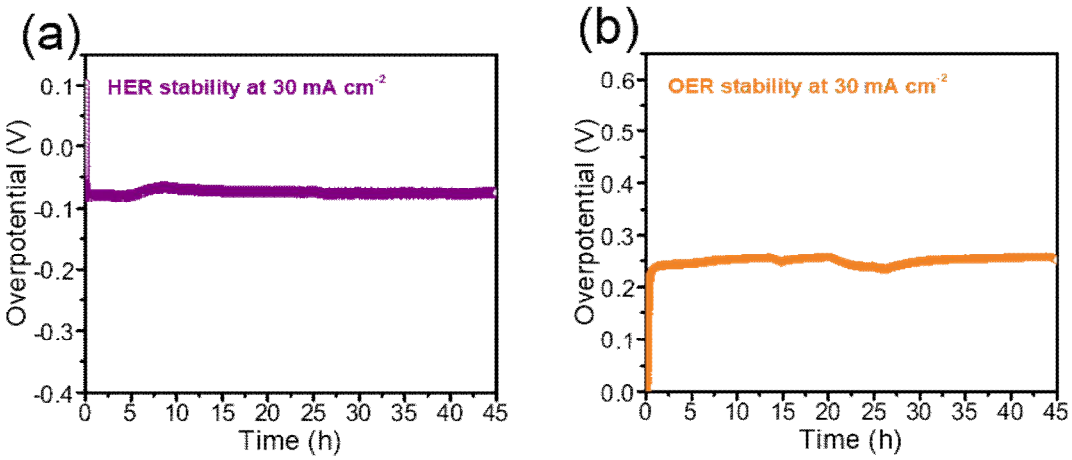

Figure. 33. The stability of the half-reaction for 45 h (a) toward HER, and (b) toward OER.

C. Two-electrode system for overall water splitting and stability test

Firstly, the two optimized Co-N-C electrode are combined to confirm the overall water splitting in alkaline electrolyte. In Figure. 34a, the LSV curves exhibits the overpotential only 1.51 V to product a current desnity of 10 mA cm^{-2}. In our study, the bi-functional Co-N-C electrode has one of the state of the art electrocatalysts,. (Table. 1) [41 - 52] The *c-t* test is conducted at a 30 mA cm^{-2} for 300 h, in Figure. 34b. The initial voltage of ~ 1.61 V is maintained significant change for 300 h, corresponding to the superior stability of the Co-N-C cataylsts.

Secondly, we confirm the change of the morphology after *c-t* test toward HER. As shown in Figure. 35, the Co-N-C microfibers are coverd with metallic nanosheets, indicating an exposed cobalt species reduced during the *c-t* test for HER. In contrast, there is no significant change of the morphology after the *c-t* test toward OER. These are confirmed again by the XRD pattern in Figure. 36. The role of Co-N_x and Co-NPs should be studied in terms of the initial activity well-preserved after the *c-t* test. As we know, the Co-N-C-1000 activity of HER and OER is not reduced despite of the presence of Co-NPs of the 100 nm upper scale by the high temperature during the annealing process. In addition, The Co-NPs are aggregated by an intermediate annealing temperature at 350 ^{o}C, following that the reduced bi-functional performances are not confirmed in Figure. 38. Furthermore, the Co-N-C electrode is washed with H_2SO_4 soluiton to leach out Co-NPs for 1 h at a room temperature. The Co-NPs are washed by the acidic solution (Figure. 39a-d, but Co-atoms are coordinated with around nitrogen or carbon. (Figure. 39e) The strength of Co-N-C test is not weakend after *c-t*, although, the activities of bi-functional performance is reduced by absence of Co-NPs, as shown in Figure. 40. The activities of HER (~ 50 mV cm^{-2}) and OER (~ 100 mV cm^{-2}) are confirmed, respectively. For this reason, the Co-NPs and Co-atoms generate a synergistic effect for the bi-functional performances.

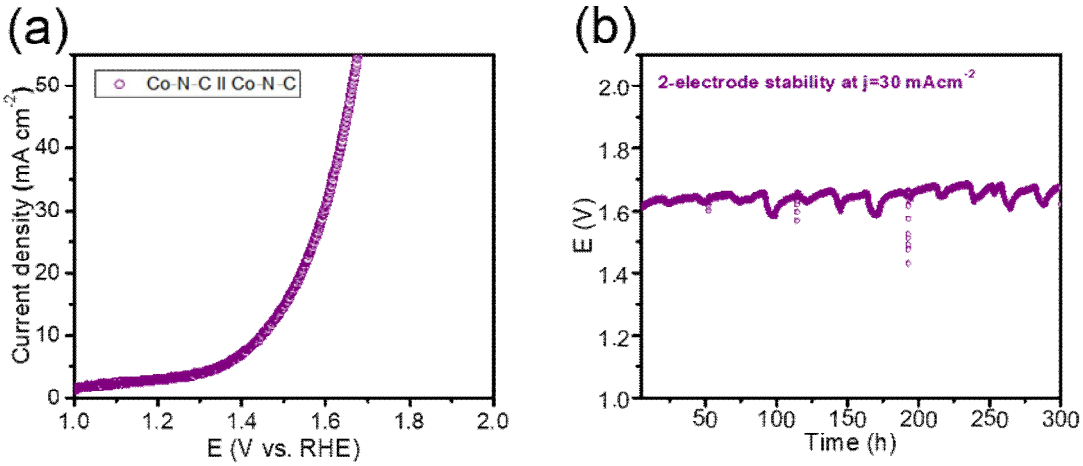

Figure. 34. (a) LSV curve of 2-electrode system consist of Co-N-C membrane, (b) long-term stablity test of Co-N-C.

ElectroCatalyst	HER η at j=10 mA cm^{-2} (mV)	OER η at j=10 mA cm^{-2} (mV)	OWS V at j=10 mA cm^{-2} (V)	reference
NCNT-NP@NF	96.1	240	1.54	Chem. Eng. J., in press (2020) 127531
Ni-MoC@NCNT/CCs	70	219	1.535	Chem. Eng. J., 406 (2021) 126815
NiFeP/SG*	115	218	1.54	Nano Energy, 58 (2019) 870-876
C-(Fe-Ni)P@PC/(Ni-Co)P@CC	142	251	1.63	Nano Energy, 65 (2019) 103995
N-NiCoP/NCF	78	225	1.56	Appl. Catal. B- Environ., 254 (2019) 414-423
CoFe-PBA NS@NF-24	48	256	1.545	Nano Energy, 68 (2020) 104371
FeOOH/Ni3N	67	244	1.58	Appl. Catal. B- Environ., 269 (2020) 118600
Co@N-CS/N-HCP@CC	66	248	1.545	Adv. Energy Mater., 9 (2019) 1803918
Cu0.3Co2.7P/NC	220	190	1.64	Adv. Energy Mater., 7 (2017) 1601555
HNDCM-100,000-1,000/Co*	158	199	-	Nat Commun, 8 (2017) 13592
Co-MoS2/BCCF-21	48	260	1.55	Adv. Mater., 30 (2018) 1801450
Co3Se4/CF	320	179	1.59	Adv. Energy Mater., 7 (2017) 1602579
Co-N-C monolithic electrode*	36	229	1.51	This work

Table 1. Overall water splitting (OWS) value of non-metal based electrocatalyst for comparison.

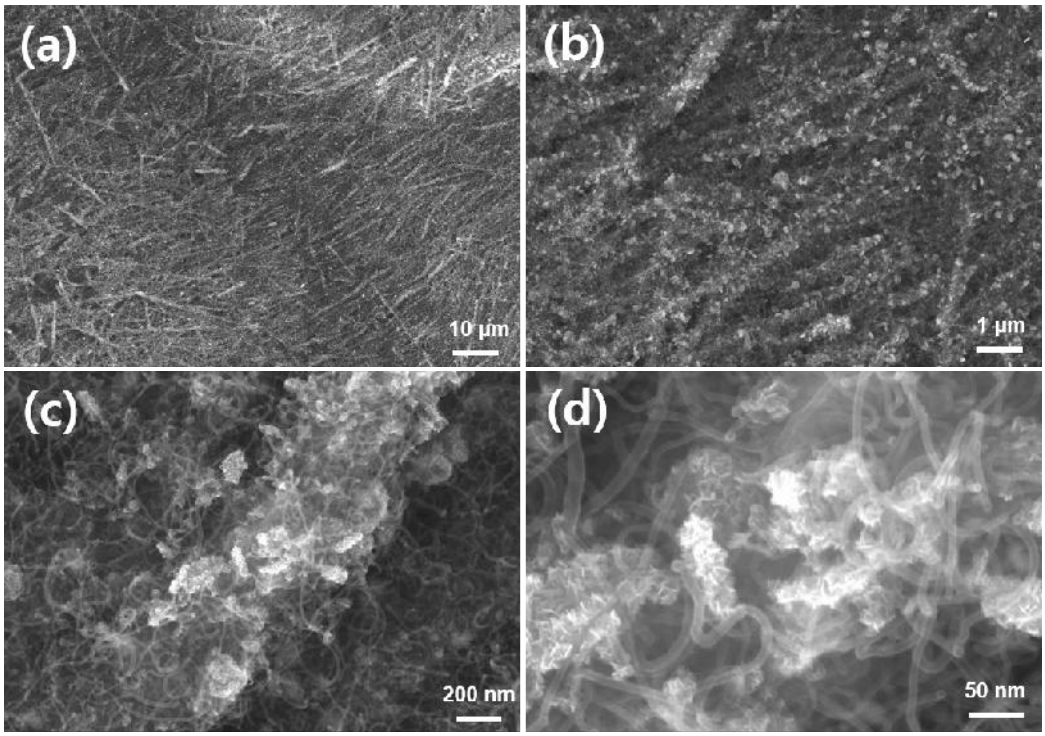

Figure. 35. SEM images of Co-N-C after the *c-t* test toward HER.

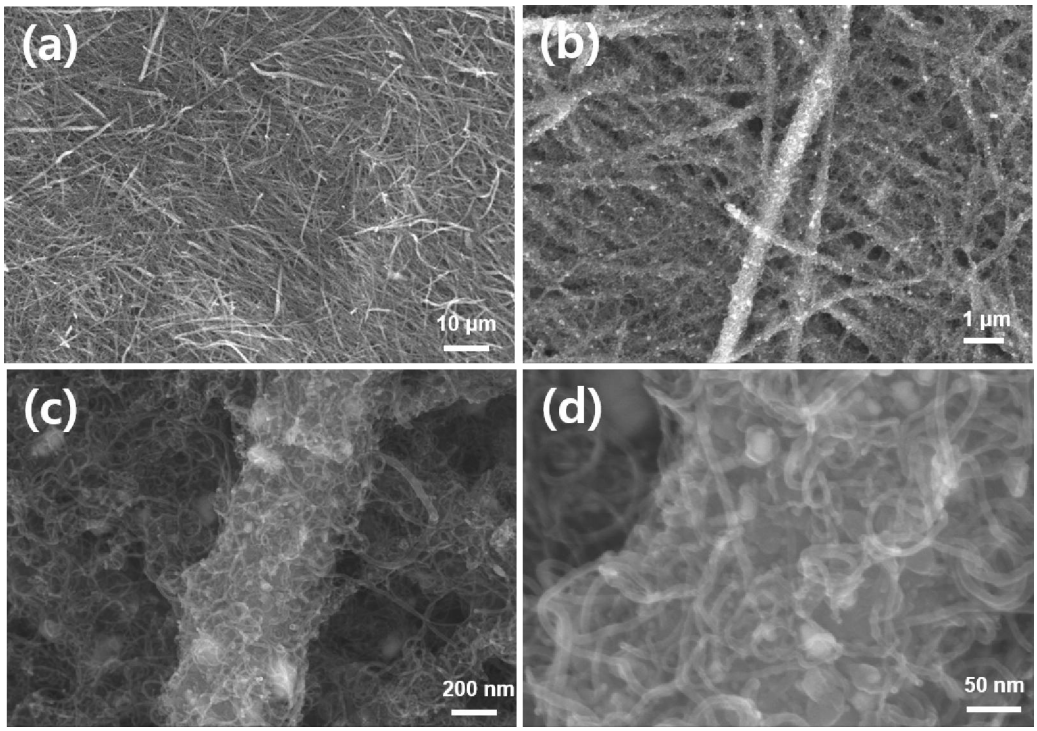

Figure. 36. SEM images of Co-N-C after the *c-t* test toward OER.

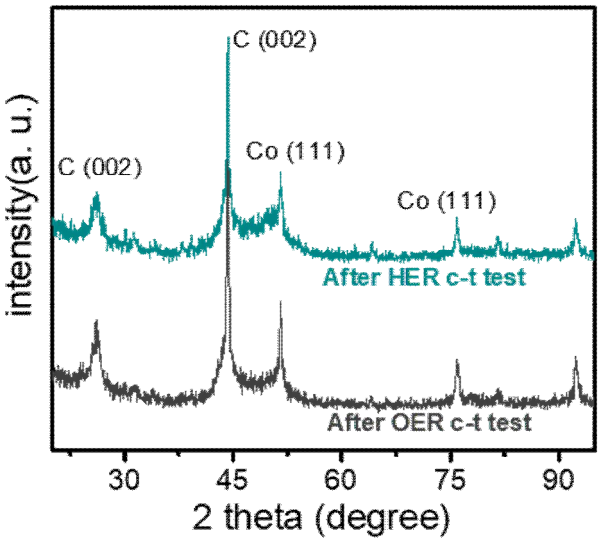

Figure. 37. XRD pattern after HER, and OER *c-t* test.

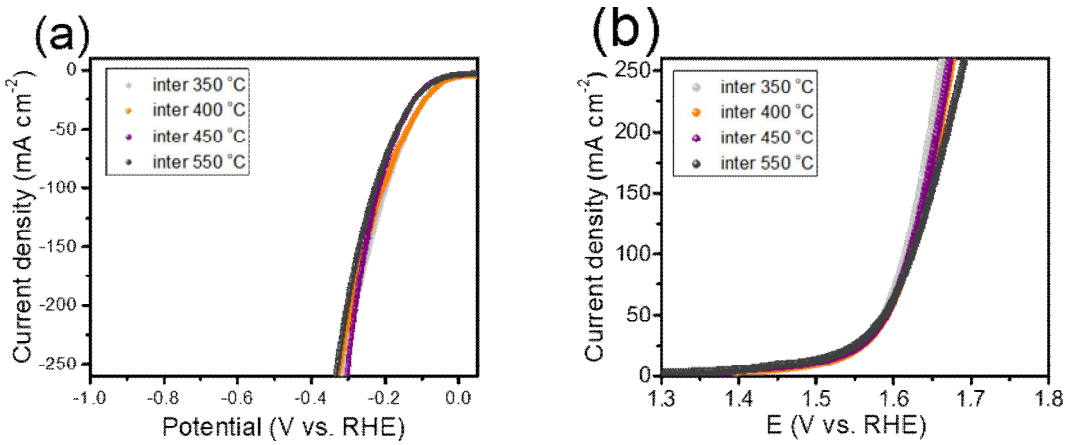

Figure. 38. LSV curves of Co-N-C after annealing process with various intermediate temperature. (a) toward HER, (b) toward OER.

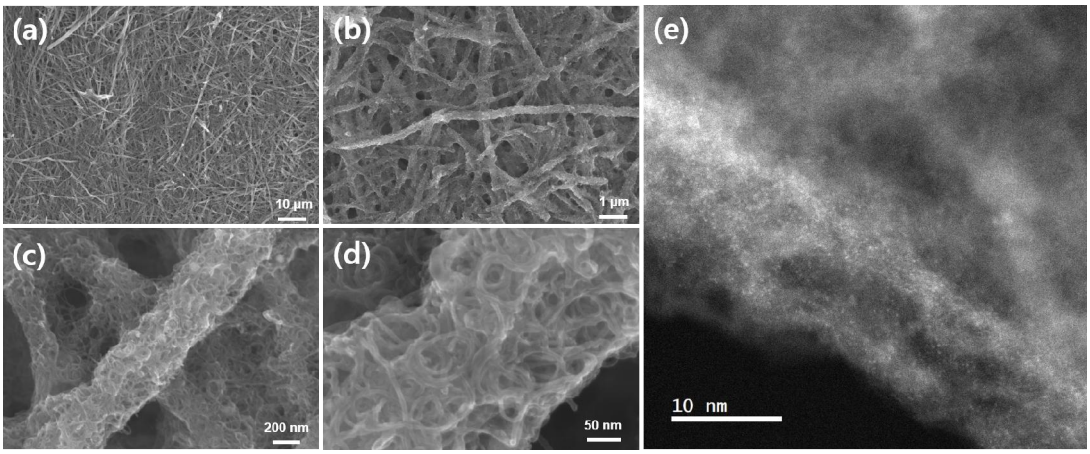

Figure. 39. (a)-(d) The various resolution SEM images, (e) STEM image of etched Co-N-C by acidic solution.

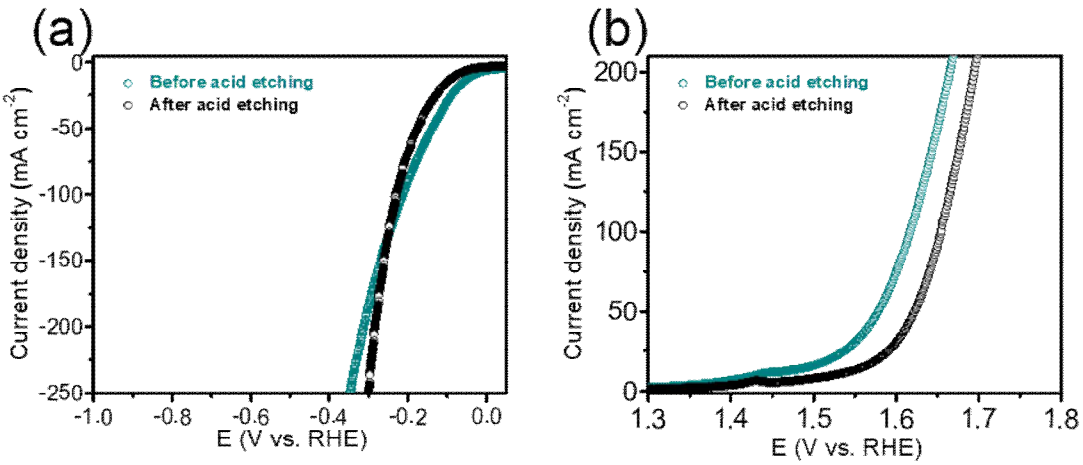

Figure. 40. LSV curves of Co-N-C before/after acid etching process. (a) toward HER, and (b) toward OER.

D. The performance of Co-N-C toward oxygen reduction reaction (ORR)

All of ORR test are producted in the O_2-saturated 0.1 M KOH solution. The catalysts prepared at the different temperature are evaluated scan rate of 1 mV s-1 in rotating ring-disk electrode (RRDE) experiments. At first, the Co-N-C electrode suffered from 600 ^oC annealing temperature exhibits the lowest activity among the electrodes with a half-wave potential ($E_{1/2}$) of 0.81 V, compared to other samples ($E_{1/2}$ = 0.82 ~ 0.858 V), in Figure. 41. As shown in Figure. 42, the Co-N-C electrode has efficient half-wave potential of 0.858 V, which is simliar performace compared to the benchmarking electrode of Pt/C ($E_{1/2}$ = 0.840 V). In our study, the various electrocatalysts are evaluated of bi-/tri- functional performance and confirmed of excellent performance compared to noble-based electrocatalysts to utilize the overall water splitting and zinc-air batteries. So, the state of the art electrodcatalysts for tri-functional performance are summarized to compare with Co-N-C electrocatalyst. (Table. S2) [20, 53-61]

In Figure 42b, the Tafel plot exhibits the value of 67.8 mV dec^{-1} with Co-N-C that is excellent charge transfer compare to the Pt/C (100.6 mV dec^{-1}) and the Co-O_x (122.3 mV dec^{-1}) electrode. The electron transfer number is evaluated by the Kouteky-Levich equation from LSV curves, the value of transfer number that is ~ 3.96 indicating a four-electron pathway. (Figure. 43) Likewise, the electron transfer number of Pt/C (3.98) and Co-O_x (3.91) are calculated from RRDE curves in Figure. 42c. The hydroxide yield of Co-N-C calculated to be ~ 5.4 %. This value of hydroxide yield is similar to Pt/C, and performed to investigate an accelerated durability test (ADT) by the cycle voltammetry in a range of potential 0.6 – 1.0 V_{RHE} with scan rate of 50 mV s^{-1} for 5000 cycles. In conclusion, the no significant chage of the potential is observed after ADT 5000 cycles.

The exceptional performance of Co-N-C can be explained with two path. At first, the co-existance of atom size Co coordinated N (Co-N_x) and Co-clusters embbed on the surface of CNTs for synergistic effect for the electrochemical reaction, has been reported the catalysts based on transitional metal by the density functional theory

(DFT). Unfortunately, these tri-functional catalysts face to face the gap of mono-functional catalysts. Recently, the single atom catalysts (SACs) with metal clusters can be improve the performance of electrocatalyst for the catalytic activities. [41, 62] The existance of Co-atoms and Co-clusters is promote the good electronic conductivity, favorable with intermediate, eliminating the drawback of SACs by the well-constructed hierachical structure.

Secondly, the Co-N-C membrane consist of well-interwined CNTs is utilized for the electrochemical reactiom such as HER, OER, and ORR, following the hard properties. The conventional method for the electrocatalyst is using the substrate, according to increasing the interfacial and ohmnic resistance. The hard property of Co-N-C electrode can be used to directly with ZABs such as a air cathode. The hierachical porous structure of the air catalyst has been proven to increase the performance for the charge/discharge reaction of ZABs.

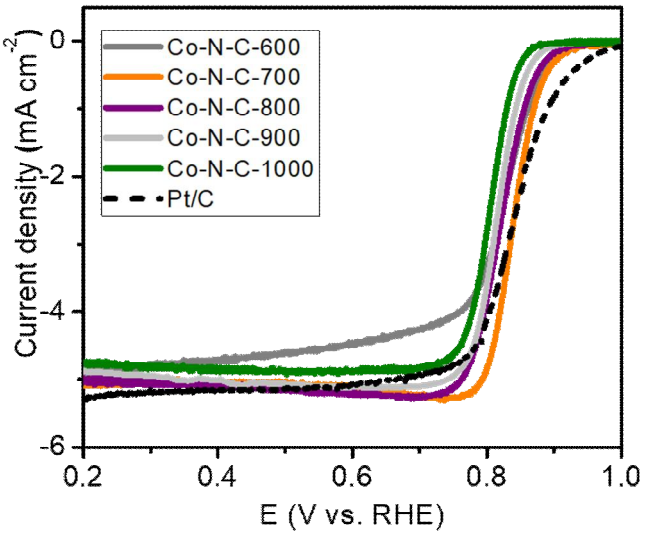

Figure. 41. LSV curves of various Co-N-C electrodes toward ORR with rotating rate of 1600 bpm.

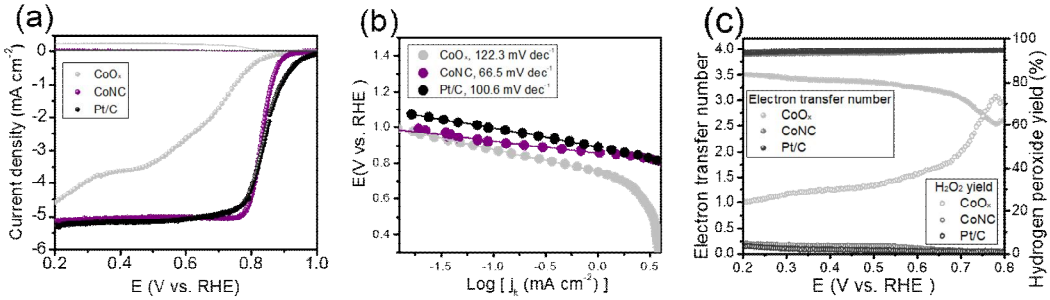

Figure. 42. (a) LSV curves of various Co-N-C electrodes toward ORR with rotating rate of 1600 rpm, (b) Tafel plot of (a), and (c) yield of hydrogen peroxide and electron transfer number of Co-N-C and Pt/C.

ElectroCatalyst	HER η at j=10 mA cm^{-2} (mV)	OER η at j=10 mA cm^{-2} (mV)	ORR half-wave potential (V)	reference
FeNiP/NPCS	126	318	0.84	Chem. Eng. J., 389 (2020) 124408
NiCoOS	300	470	0.79	Nano Energy, 58 (2019) 680-686
CoNx/NGA	198	295	0.83	Appl. Catal. B- Environ., 259 (2019) 118100
Co4N@NC-2	283	290a	0.842	Appl. Catal. B- Environ., 275 (2020) 119104
CoOx/CoNy@CNz,700	261.4	280	0.83	Appl. Catal. B- Environ., 279 (2020) 119407
FeCoMoS@NG	137	238	0.83	Appl. Catal. B- Environ., 279 (2020) 119381
CuF@CuCoNC-500	59	245	0.84	Appl. Catal. B- Environ., 263 (2020) 118139
DG	320	340	0.760	Adv. Mater., 28 (2016) 9532-9538
MSZIF-900	233b	337	0.84	Angew. Chem. Int. Ed., 56 (2017) 13781-13785
Fe-N4 SAs/NPC	430	202	0.885	Angew. Chem. Int. Ed., 57 (2018) 8614-8618
Co-N-C monolithic electrode	36	229	0.858	This work

Table 2. Tri-functional non-noble metal based electrocatalysts to compare with Co-N-C, the electrolyte for the overall water splitting using 1 M KOH and for the ORR using 0.1 M KOH, basically. The other cases such as 0.1 M KOH for the HER/OER, indicating "a", and 0.5 M H_2SO_4 for the ORR, indicating "b", respectively.

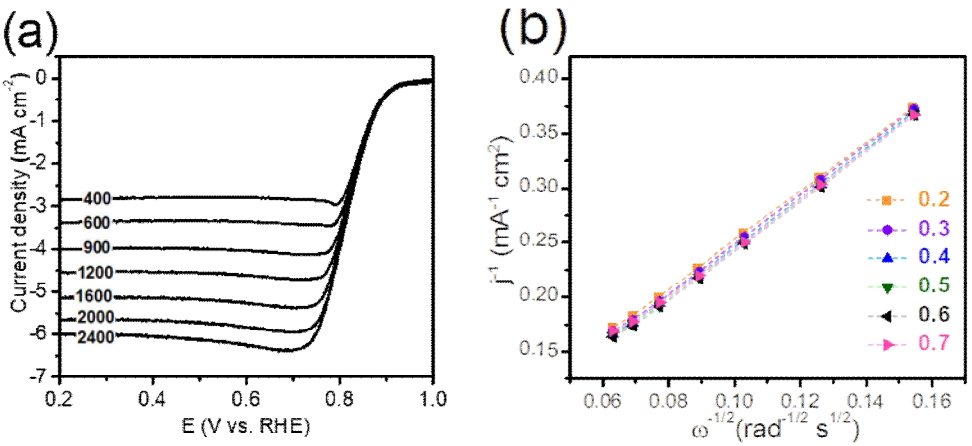

Figure. 43. (a) LSV curves of various Co-N-C electrodes toward ORR with different rotating rate from 400 to 2000 rpm, (b) Calculated electron transfer number by Koutecky-Levich equation from (a).

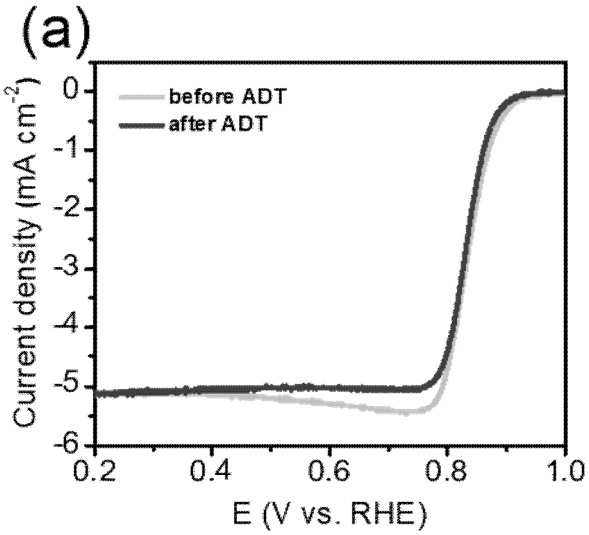

Figure. 44. (a) LSV curves of various Co-N-C electrodes toward ORR before ADT, and after ADT for 5000 cycles.

E. Overall water splitting and Zinc-air batteries with Co-N-C electrode

In ZABs, the OER and ORR are critical reaction for the charging or discharging. Therefore, the performance of air cathode is using the indicator of ZABs cyclic performance. The air cathode fabricated by the Co-N-C powder of 1 mg cm^{-2} is deposited onto the carbon nanofibers paper and the Pt/C is fabricated with the same methode for comparing. And then, the liquid-type ZABs are assembled using the 6 M KOH electrolyte containing 0.2 M $ZnCl_2$, using the Zn plate for the anode, and using the Co-N-C membrane for the cathode. The charging/discharging polarization profiles of ZABs assembled with Co-N-C or Pt/C air cathode, respectively. The ZABs consist of Co-N-C is showing the smaller voltage gap between charging and discharging, compared to the Pt/C air cathode ZABs. The maximum power density of the ZABs based on the air cathode of Co-N-C evaluated of the 181.3 mW cm^{-2}, and Pt/C air cathode ZABs is 116.3 mV cm^{-2}. The Co-N-C ZABs is much higher than Pt/C air cathode ZABs. The rechargable ZABs at current density of 5 mA cm^{-2} is cycled over 1320 cycles with a periods of 30 s between charging and discharging, corresponding to 110 h. The voltage gap of ZABs assembled by Co-N-C for the air cathode is 0.92 V (2.10 to 1.18 V for charging and discharging potential). In contrast, the Pt/C air cathode of ZABs is exhibits the voltage gap of 1.1 V (2.27 to 1.17 V), which higher potential than Co-N-C. (Figure. 45b) The voltage gap of Co-N-C increase slightly during the 110 h, corresponding to potential of 0.97 V, while the Pt/C ZABs is increased severely, indicating the Pt/C particles on the carbon substrate are agglomeratated or leached out during the charging reaction (OER).

In terms of hard property, the Co-N-C air cathode can be utilized directly for the all-solid-state electrolyte rechargble ZABs. As shown in Figure. 45c, the rechargable ZABs with solid-electrolyte is assembled with Zn foil for anode, poly(vinyl alcohol) (PVA) gel containing KOH for electrolyte. In Figure. 45d, the ZABs assembled by Pt/C exhibits the voltage gab of ~ 1.1 V, while the ZABs with Co-N-C exhibits the much smaller voltage gap of ~ 0.5 V. The cycling test is conducted at the current density of 5 mA cm^{-2} assembled with Pt/C that can be lost their activity easily within 1 h. This

rapid loss of activity can be explained probably in terms of degration from carbon substrate and/or exposed gel-type electrolyte at the air, which is recoverd by the addition of water in the gel-electrolyte using a pipette in Figure. 46. The sealing with Teflon-tape the gel-electrolyte to prevent the moisture, leading to dramatically reduced the voltage gap between charge and discharge potential compared to non-sealing ZABs. Contributed to the well-made hierachical structure, lead to the highly efficient battery performance at the gel-type ZABs by a large number of active sites and the facile mass transfer. These excellent durability and performance is compared to the recently reported state-of-the-art ZABs. (Table 3) [19, 56, 58, 62-68]

Finally, a self-powered water splitting system is explained by connecting the alkaline water electrolyzer and the ZABs. (Figure. 47) [17, 67, 68] The power source of ZABs using the zinc foil, in the gel-type ZABs, the monolithic Co-N-C membrane fabricated by annealing process with an appropriate temperature is used directly as the air cathode and water electrolyzer. As shown in Figure. 48, the faradaic efficiency of the production H_2 and O_2 is calculated about 97 % compared to the theorical and practical, the ratio of H_2 : O_2 = 2 : 1, close to the theorical amount of H_2, O_2. These results explain the high efficiency, multi-funcional electorde of Co-N-C by the monolith of CNTs. The Co-N-C electrode can satisfy that perform as a catalyst for the electrochemical reaction as energy conversion and storage system.

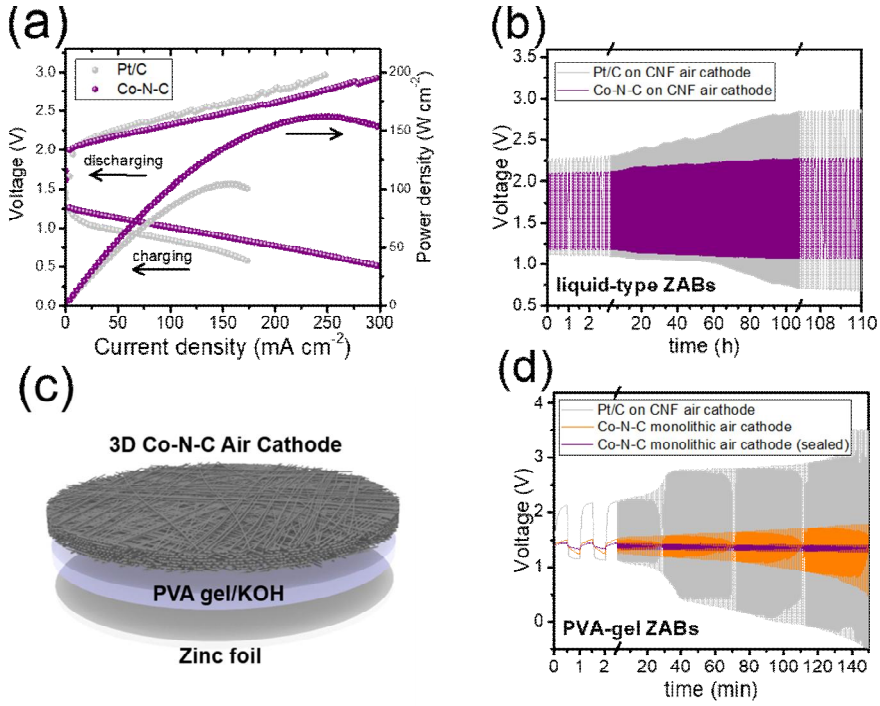

Figure. 45. (a) The charge and discharge polarization of ZABs with air cathode of Pt/C and Co-N-C on the carbon paper. (b) Cyclic performance with liquid electrolyte of Pt/C and Co-N-C batteries. (c) Schematic illustration of all-solid-state ZABs. (d) Cyclic performance with gel-type electrolyte batteries.

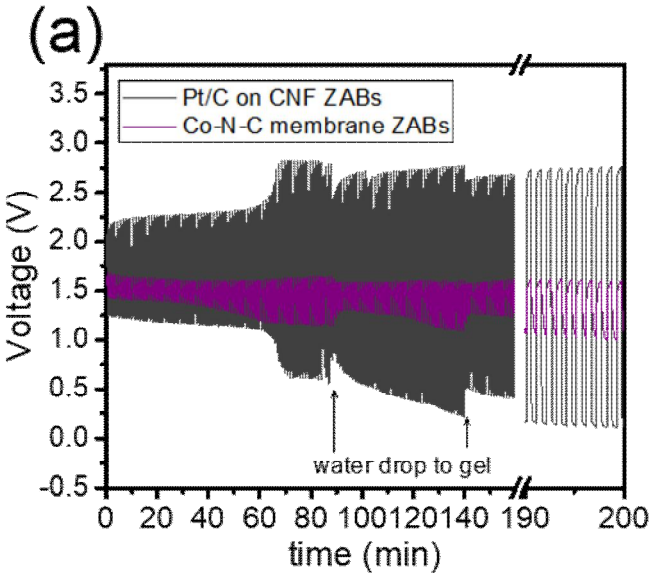

Figure. 46. (a) The recovering effect by the drop-let of the water in the gel-electrolyte at the ZABs.

Air Electrode	The type of Electrolyte	Peak power density (mWcm-2)	initial voltage gap (ΔV)	Cycle conditions	reference
Co2P/CoN-in-NCNTs	liquid	194.6	1.1	96 h at 5 mA cm^{-2}	Adv. Funct. Mater., 28 (2018) 1805641
Co-Co3O4@NAC	liquid	164	0.791	35 h at 10 mA cm^{-2}	Appl. Catal. B- Environ., (2020) 118188
FeCoMoS@NG	liquid	118	0.77	70 h at 2 mA cm^{-2}	Appl. Catal. B- Environ., 279 (2020) 119381
Co/CoS/Fe-HSNC-700	liquid	213	0.79	50 h at 2 mA cm^{-2}	Chemical Engineering Journal 403 (2021) 126385
CoP@PNC-DoS	liquid	138.57	0.94	170 h at 30 mA cm^{-2}	Energy Storage Materials 28 (2020) 27–36
Co3O4/Co@NCs	liquid	123.5	0.89	600 h at 10 mA cm^{-2}	Nano Energy 2020, 77, 105200
NOGB-800	liquid	111.9	0.72	30h at 10 mA cm^{-2}	Adv. Energy Mater. 2019, 9, 1803867
FeCo/Co2P@NPCF	liquid	154	0.83	107 h at 10 mA cm^{-2}	Adv. Energy Mater., 2020, 10, 1903854
Co4N@NC-2	liquid	74.3	0.89	750 h at 5 mA cm^{-2}	Appl. Catal. B- Environ., 275 (2020) 119104
	PVA gel	-	0.69	42 h at 2 mA cm^{-2}	
CoSx/Co-NC-800	liquid	103	0.73	100 h at 2 mA cm^{-2}	Adv. Funct. Mater. 2019, 29, 1904481
	PVA gel	-	0.54	1000 min at 1 mA cm^{-2}	
Co-N-C	liquid	181.3	0.92	110 h at 5 mA cm^{-2}	this work
	PVA gel	-	0.5	140 min at 5 mA cm^{-2}	

Table 3. Comparion of the state-of-the-art ZABs with the Co-N-C batteries. The liquid electrolyte using 6 M KOH containing 0.2 M zinc acetate or zinc chloride.

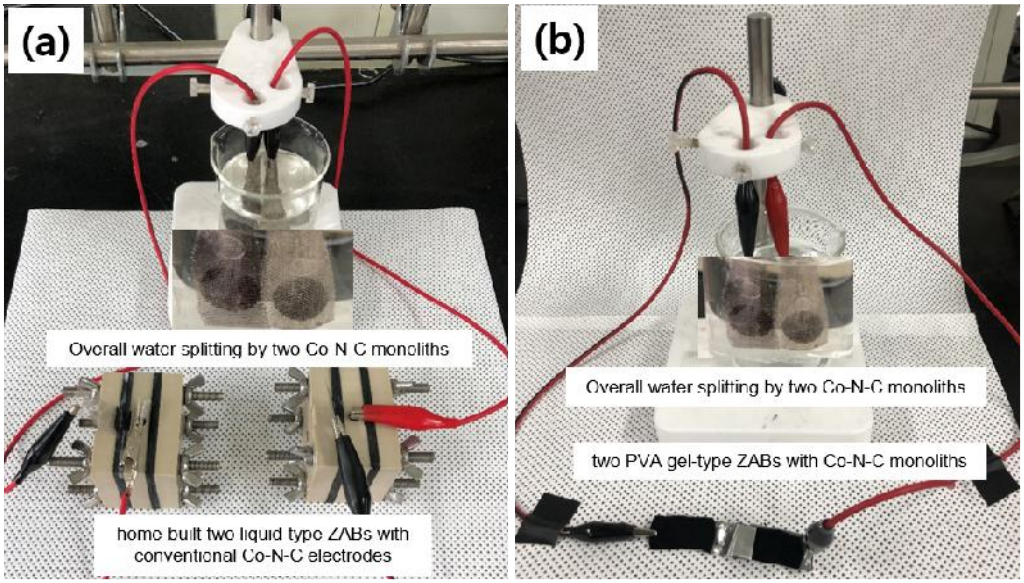

Figure. 47. Photographic images of (a) liquid-type electrolyte ZABs and (b) gel-type electrolyte ZABs connecting series for a self-powered water splitting.

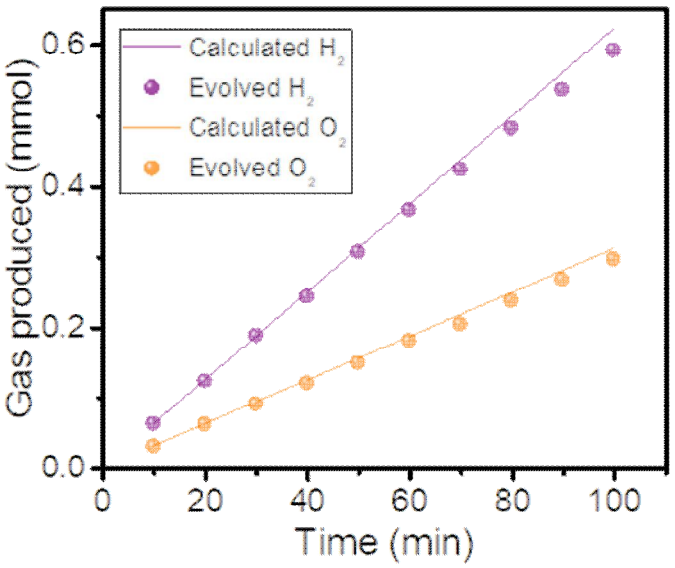

Figure. 48. Production ratio of H_2 and O_2 by the alkaline electrolyzer with 2 electrode system in 1 M KOH electrolyte at 20 mA cm^{-2}.

IV. Conclusion

In this study, as-prepared Co-M is fabricated easily by the hydrothermal method and converted as Co-N-C electrode by the annealing process with a presence of melamine. During the annealing process, the Co-N-C membrane is gained a lot of Co-clusters with Co-atoms by the Co-M consist of Co-species that dispersed onto the graphene matrix of the CNTs. The fabricated Co-N-C membrane consist of 1D hierachical structure and integrated Co nanoparticles/clusters/atoms. Firstly, the Co-N-C active sites are reconstructed by atomic Co along with the clusters. These active sites by integrated Co are used to prove a synergistic effect for multi-functional activity. The electrochemical performance of Co-N-C is exhibited more excellent compared to benchmarking noble metal based catalysts. Secondly, the 3D structure of the monolithic membrane is interwovend by the 1D structrue of Co-N-C, which exposed active sites and utilized of the pathways for mass and charge transfer. By using the well-proven CNT growth mechanism, this process of self-assembly utilizing a CNTs provides a new approach to free-standing type catalyst for electrochemical reaction, with a well designed structure consist of atoms, nanoparticles, and porous 1D hierachical carbon matrix. Finally, the monolithic Co-N-C for the reaction such as HER, OER, and ORR has superior activities compared to noble metal based catalyst. Furthermore, this monolithic catalyst can be used as alkaline water electrolyzer and ZABs.

References

[1] Sultan, S., et al. (2019). "Single Atoms and Clusters Based Nanomaterials for Hydrogen Evolution, Oxygen Evolution Reactions, and Full Water Splitting." Advanced Energy Materials 9(22)

[2] Huang, N., et al. (2019). "Cobalt-Embedded N-Doped Carbon Arrays Derived In Situ as Trifunctional Catalyst Toward Hydrogen and Oxygen Evolution, and Oxygen Reduction." ChemElectroChem **6**(17): 4522-4532.

[3] Wan, G., et al. (2020). "Toward Efficient Carbon and Water Cycles: Emerging Opportunities with Single-Site Catalysts Made of 3d Transition Metals." Adv Mater **32**(2): e1905548.

[4] Dong, X. L., et al. (2014). "Flexible and Wire-Shaped Micro-Supercapacitor Based on Ni(OH)2-Nanowire and Ordered Mesoporous Carbon Electrodes." Advanced Functional Materials **24**(22): 3405-3412.

[5] Lu, X., et al. (2020). "3D microstructure design of lithium-ion battery electrodes assisted by X-ray nano-computed tomography and modelling." Nat Commun **11**(1): 2079.

[6] Wang, Z., et al. (2018). "Fe, Cu-Coordinated ZIF-Derived Carbon Framework for Efficient Oxygen Reduction Reaction and Zinc-Air Batteries." Advanced Functional Materials **28**(39).

[7] Huang, Z.-F., et al. (2017). "Design of Efficient Bifunctional Oxygen Reduction/Evolution Electrocatalyst: Recent Advances and Perspectives." Advanced Energy Materials **7**(23).

[8] Qian, Q., et al. (2019). "Ambient Fast Synthesis and Active Sites Deciphering of Hierarchical Foam-Like Trimetal-Organic Framework Nanostructures as a Platform for Highly Efficient Oxygen Evolution Electrocatalysis." Adv Mater **31**(23): e1901139.

[9] Ahn, S. H., et al. (2017). ""Wiring" Fe-Nx -Embedded Porous Carbon Framework onto 1D Nanotubes for Efficient Oxygen Reduction Reaction in Alkaline and Acidic Media." Adv Mater **29**(26).

[10] Li, H. G., et al. (2021). "Enhanced Fe 3d delocalization and moderate spin polarization in Fe-Ni atomic pairs for bifunctional ORR and OER electrocatalysis." Applied Catalysis B-Environmental **285**.

[11] Zhang, S. Y., et al. (2021). "Template-free synthesis of non-noble metal single-atom electrocatalyst with N-doped holey carbon matrix for highly efficient oxygen reduction reaction in zinc-air batteries." Applied Catalysis B-Environmental **285**.

[12] Noor, T., et al. (2021). "Recent Advances in Electrocatalysis of Oxygen Evolution Reaction using Noble-Metal, Transition-Metal, and Carbon-Based Materials." ChemElectroChem **8**(3): 447-483.

[13] Jia, Z., et al. (2017). "Controllable and Large-Scale Synthesis of Carbon Nanostructures: A Review on Bamboo-Like Nanotubes." Catalysts **7**(9).

[14] Chhowalla, M., et al. (2013). "The chemistry of two-dimensional layered transition metal dichalcogenide nanosheets." Nat Chem **5**(4): 263-275.

[15] Xu, M., et al. (2015). "Porous CoP concave polyhedron electrocatalysts synthesized from metal-organic frameworks with enhanced electrochemical properties for hydrogen evolution." Journal of Materials Chemistry A **3**(43): 21471-21477.

[16] Ji, D., et al. (2019). "Atomically Transition Metals on Self-Supported Porous

Carbon Flake Arrays as Binder-Free Air Cathode for Wearable Zinc-Air Batteries." Adv Mater **31**(16): e1808267.

[17] Li, Y., et al. (2020). "Supramolecular assisted one-pot synthesis of donut-shaped CoP@PNC hybrid nanostructures as multifunctional electrocatalysts for rechargeable Zn-air batteries and self-poared hydrogen production." Energy Storage Materials **28**: 27-36.

[18] Burke, M. S., et al. (2015). "Cobalt-Iron (Oxy)hydroxide Oxygen Evolution Electrocatalysts: The Role of Structure and Composition on Activity, Stability, and Mechanism." Journal of the American Chemical Society **137**(10): 3638-3648.

[19] Zhong, X., et al. (2020). "Co single-atom anchored on Co3O4 and nitrogen-doped active carbon toward bifunctional catalyst for zinc-air batteries." Applied Catalysis B: Environmental **260**.

[20] Pan, Y., et al. (2018). "A Bimetallic Zn/Fe Polyphthalocyanine-Derived Single-Atom Fe-N-4 Catalytic Site:A Superior Trifunctional Catalyst for Overall Water Splitting and Zn-Air Batteries." Angewandte Chemie-International Edition **57**(28): 8614-8618.

[21] He, T. W., et al. (2019). "Transition-Metal Single Atoms Anchored on Graphdiyne as High-Efficiency Electrocatalysts for Water Splitting and Oxygen Reduction." Small Methods **3**(9).

[22] Qin, Q., et al. (2019). "A Tannic Acid-Derived N-, P-Codoped Carbon-Supported Iron-Based Nanocomposite as an Advanced Trifunctional Electrocatalyst for the Overall Water Splitting Cells and Zinc-Air Batteries." Advanced Energy Materials **9**(5).

[23] Jia, Z.; Kou, K.; Qin, M.; Wu, H.; Puleo, F.; Liotta, L., Catalysts 2017.

[24] Zhao, X. and N. Yan (2015). "One-pot synthesis and assembly of melamine-based nanoparticles for microporous polymer organic frameworks and their application as a support for a silver nanoparticle catalyst." RSC Advances **5**(86): 69955-69961.

[25] Faisal, S. N., et al. (2017). "Pyridinic and graphitic nitrogen-rich graphene for high-performance supercapacitors and metal-free bifunctional electrocatalysts for ORR and OER." RSC Advances **7**(29): 17950-17958.

[26] Tian, K., et al. (2020). "Single-site pyrrolic-nitrogen-doped sp(2)-hybridized carbon materials and their pseudocapacitance." Nat Commun **11**(1): 3884.

[27] Cheng, N., et al. (2020). "In-situ grafting of N-doped carbon nanotubes with Ni encapsulation onto MOF-derived hierarchical hybrids for efficient electrocatalytic hydrogen evolution." Carbon **163**: 178-185.

[28] Xu, Y. A., et al. (2014). "Effect of the length and surface area on electrochemical performance of cobalt oxide nanowires for alkaline secondary battery application." Journal of Power Sources **272**: 703-710.

[29] Li, C. C., et al. (2012). "Synthesis of highly aligned and ultralong coordination polymer nanowires and their calcination to porous manganese oxide nanostructures." Journal of Materials Chemistry **22**(11): 4982-4988.

[30] Zhang, Y. K., et al. (2018). "Atomic Iridium Incorporated in Cobalt Hydroxide for Efficient Oxygen Evolution Catalysis in Neutral Electrolyte." Advanced Materials **30**(18).

[31] Z. Liu, R. Ma, M. Osada, K. Takada, T. Sasaki, Selective and controlled synthesis of α- and β-cobalt hydroxides in highly developed hexagonal platelets, J. Am. Chem. Soc. 127 (40) (2005) 13869−13874

[32] Yang, Z., et al. (2019). "Trifunctional Self-Supporting Cobalt-Embedded Carbon Nanotube Films for ORR, OER, and HER Triggered by Solid Diffusion from Bulk Metal." Adv Mater **31**(12): e1808043.

[33] Jiang, W. J., et al. (2016). "Understanding the High Activity of Fe-N-C Electrocatalysts in Oxygen Reduction: Fe/Fe3C Nanoparticles Boost the Activity of Fe-N-x." Journal of the American Chemical Society **138**(10): 3570-3578.

[34] Liu, L., et al. (2018). "Growth-Oriented Fe-Based MOFs Synergized with Graphene Aerogels for High-Performance Supercapacitors." Advanced Materials Interfaces **5**(8).

[35] Lu, Q., et al. (2019). "Self-Catalyzed Growth of Co, N-Codoped CNTs on Carbon-Encased CoSx Surface: A Noble-Metal-Free Bifunctional Oxygen Electrocatalyst for Flexible Solid Zn-Air Batteries." Advanced Functional Materials **29**(38)

[36] Hou, C. C., et al. (2019). "A Hydrangea-Like Superstructure of Open Carbon Cages with Hierarchical Porosity and Highly Active Metal Sites." Advanced Materials **31**(46).

[37] Wu, C., et al. (2016). "Peapod-Like Carbon-Encapsulated Cobalt Chalcogenide Nanowires as Cycle-Stable and High-Rate Materials for Sodium-Ion Anodes." Adv Mater **28**(33): 7276-7283.

[38] Wu, K., et al. (2020). "An Iron-Decorated Carbon Aerogel for Rechargeable Flow and Flexible Zn-Air Batteries." Adv Mater: e2002292.

[39] Chen, Y. Y., et al. (2017). "Self-Templated Fabrication of MoNi4 /MoO3-x Nanorod Arrays with Dual Active Components for Highly Efficient Hydrogen Evolution." Adv Mater **29**(39).

[40] Li, W., et al. (2019). "Hydrogen evolution reaction mechanism on 2H-MoS2 electrocatalyst." Applied Surface Science **498**.

[41] Cheng, Y., et al. (2021). "Self-supported bifunctional electrocatalysts with Ni nanoparticles encapsulated in vertical N-doped carbon nanotube for efficient overall water splitting." Chemical Engineering Journal **413**.

[42] Geng, B., et al. (2021). "Ni/MoC heteronanoparticles encapsulated within nitrogen-doped carbon nanotube arrays as highly efficient self-supported electrodes for overall water splitting." Chemical Engineering Journal **406**.

[43] Li, R. Q., et al. (2019). "Monolithic electrode integrated of ultrathin NiFeP on 3D strutted graphene for bifunctionally efficient overall water splitting." Nano Energy **58**: 870-876.

[44] Lv, C. N., et al. (2019). "Double functionalization of N-doped carbon carved hollow nanocubes with mixed metal phosphides as efficient bifunctional catalysts for electrochemical overall water splitting." Nano Energy **65**.

[45] Zhang, R., et al. (2019). "In situ engineering bi-metallic phospho-nitride bi-functional electrocatalysts for overall water splitting." Applied Catalysis B-Environmental **254**: 414-423.

[46] Chen, Z. L., et al. (2020). "Ultrathin Prussian blue analogue nanosheet arrays with open bimetal centers for efficient overall water splitting." Nano Energy **68**.

[47] Guan, J. L., et al. (2020). "FeOOH-enhanced bifunctionality in Ni3N nanotube arrays for water splitting." Applied Catalysis B-Environmental **269**.

[48] Chen, Z., et al. (2019). "Oriented Transformation of Co-LDH into 2D/3D ZIF-67 to Achieve Co–N–C Hybrids for Efficient Overall Water Splitting." Advanced Energy

Materials **9**(19).

[49] Song, J., et al. (2017). "Bimetallic Cobalt-Based Phosphide Zeolitic Imidazolate Framework: CoPxPhase-Dependent Electrical Conductivity and Hydrogen Atom Adsorption Energy for Efficient Overall Water Splitting." Advanced Energy Materials **7**(2).

[50] Wang, H., et al. (2017). "Synthesis of single-crystal-like nanoporous carbon membranes and their application in overall water splitting." Nat Commun **8**: 13592.

[51] Xiong, Q., et al. (2018). "Cobalt Covalent Doping in MoS2 to Induce Bifunctionality of Overall Water Splitting." Adv Mater: e1801450.

[52] Li, W., et al. (2017). "Hydrothermal Synthesis of Monolithic Co3Se4 Nanowire Electrodes for Oxygen Evolution and Overall Water Splitting with High Efficiency and Extraordinary Catalytic Stability." Advanced Energy Materials **7**(17).

[53] Ren, J. T., et al. (2020). "Binary FeNi phosphides dispersed on N,P-doped carbon nanosheets for highly efficient overall water splitting and rechargeable Zn-air batteries." Chemical Engineering Journal **389**.

[54] Bai, Z. Y., et al. (2019). "Metal-organic framework-derived Nickel Cobalt oxysulfide nanocages as trifunctional electrocatalysts for high efficiency power to hydrogen." Nano Energy **58**: 680-686.

[55] Zou, H. Y., et al. (2019). "In situ coupled amorphous cobalt nitride with nitrogen-doped graphene aerogel as a trifunctional electrocatalyst towards Zn-air battery deriven full water splitting." Applied Catalysis B-Environmental **259**.

[56] Ge, H., et al. (2020). "Co4N nanoparticles encapsulated in N-doped carbon box as tri-functional catalyst for Zn-air battery and overall water splitting." Applied Catalysis

B: Environmental **275**.

[57] Liu, J., et al. (2020). "CoOx/CoNy nanoparticles encapsulated carbon-nitride nanosheets as an efficiently trifunctional electrocatalyst for overall water splitting and Zn-air battery." Applied Catalysis B: Environmental **279**.

[58] Ramakrishnan, S., et al. (2020). "Nitrogen-doped graphene encapsulated FeCoMoS nanoparticles as advanced trifunctional catalyst for water splitting devices and zinc−air batteries." Applied Catalysis B: Environmental **279**.

[59] Sun, H., et al. (2020). "Highly efficient water splitting driven by zinc-air batteries with a single catalyst incorporating rich active species." Applied Catalysis B-Environmental **263**.

[60] Jia, Y., et al. (2016). "Defect Graphene as a Trifunctional Catalyst for Electrochemical Reactions." Adv Mater **28**(43): 9532-9538.

[61] Jia, G., et al. (2017). "Three-Dimensional Hierarchical Architectures Derived from Surface-Mounted Metal-Organic Framework Membranes for Enhanced Electrocatalysis." Angewandte Chemie-International Edition **56**(44): 13781-13785.

[62] Lei, C. J., et al. (2019). "Efficient alkaline hydrogen evolution on atomically dispersed Ni-Nx Species anchored porous carbon with embedded Ni nanoparticles by accelerating water dissociation kinetics." Energy & Environmental Science **12**(1): 149-156.

[63] Guo, Y., et al. (2018). "Co2P-CoN Double Active Centers Confined in N-Doped Carbon Nanotube: Heterostructural Engineering for Trifunctional Catalysis toward HER, ORR, OER, and Zn-Air Batteries Driven Water Splitting." Advanced Functional Materials **28**(51).

[64] Yan, L., et al. (2021). "Formation of mesoporous Co/CoS/Metal-N-C@S, N-codoped hairy carbon polyhedrons as an efficient trifunctional electrocatalyst for Zn-air batteries and water splitting." Chemical Engineering Journal **403**.

[65] Yu, N.-F., et al. (2020). "Highly efficient Co3O4/Co@NCs bifunctional oxygen electrocatalysts for long life rechargeable Zn-air batteries." Nano Energy **77**.

[66] Hu, Q., et al. (2019). "Trifunctional Electrocatalysis on Dual-Doped Graphene Nanorings-Integrated Boxes for Efficient Water Splitting and Zn-Air Batteries." Advanced Energy Materials **9**(14).

[67] Shi, Q., et al. (2020). "High-Performance Trifunctional Electrocatalysts Based on FeCo/Co2P Hybrid Nanoparticles for Zinc−Air Battery and Self-Powered Overall Water Splitting." Advanced Energy Materials **10**(10).

[68] Zhang, J. T. and L. M. Dai (2016). "Nitrogen, Phosphorus, and Fluorine Tri-doped Graphene as a Multifunctional Catalyst for Self-Powered Electrochemical Water Splitting." Angewandte Chemie-International Edition **55**(42): 13296-13300.